Computational and Theoretical Chemistry 1257 (2026) 115663

Contents lists available at ScienceDirect

Computational and Theoretical Chemistry

journal homepage: www.elsevier.com/locate/comptc

Structural evolution and thermodynamic tuning of $Sr_{1-x}Ba_xLiH_3$: Inverse perovskites for high-volumetric-capacity hydrogen storage

S. Saadoun [a,b], T. Ghellab [a,b,*], H. Baaziz [a,b,*], T. Saadi [a,b], Z. .Charifi [a,b]

[a] Department of Physics, Faculty of Science, University of M'sila, 28000 M'sila, Algeria
[b] Laboratory of physics and chemistry of materials, University of M'sila, Algeria

ARTICLE INFO

Keywords:
Inverse perovskite hydrides
$Sr_{1-x}Ba_xLiH_3$ alloys
Hydrogen binding
Cation substitution
Desorption temperature

ABSTRACT

This computational study investigates the structure-property relationships in $Sr_{1-x}Ba_xLiH_3$ ($0 \leq x \leq 1$) inverse perovskite hydrides using DFT. We demonstrate how controlled Ba substitution systematically tunes formation energies (−60.4 to −58.8 kJ/mol·H_2) and hydrogen binding energies (−1.19 to −1.24 eV), enabling precise optimization of hydrogen storage performance. The alloys exhibit an unusual structural evolution from cubic ($Pm\bar{3}m$) to tetragonal ($P4/mmm$) and back to cubic ($Pm\bar{3}m$) symmetry, with the re-entrant cubic phase at x = 0.875 showing exceptional stability (cohesive energy −17.1 eV). Electronic structure calculations reveal composition-dependent bandgap transitions (3.45–4.13 eV, mBJ-GGA) that alternate between direct and indirect character. For hydrogen storage, the materials' key advantage lies in their outstanding volumetric capacity of 188 g H_2/L, which significantly exceeds the capacities of many benchmark storage systems, while they maintain a moderate gravimetric capacity of 2.1–3.2 wt%. Desorption temperatures (449–462 K) are directly correlated with the hydrogen binding energy landscape. The study identifies an optimal composition window (x = 0.25–0.5) that balances favorable formation energy (−59.5 kJ/mol·H_2), moderate hydrogen binding (−1.22 eV), and robust thermodynamic stability. These findings establish a quantitative framework for designing perovskite hydrides with tailored hydrogen storage properties through controlled cation substitution, specifically targeting applications where high volumetric density is a critical requirement.

1. Introduction

Projections indicate that the world's petroleum reserves could be exhausted within 41 years, while fossil fuel consumption is expected to increase by 56% by 2040, intensifying concerns over energy security and the long-term viability of environmental systems [1]. These challenges are compounded by predictions of a 2.5 °C rise in global temperatures by the century's end [2,3]. The convergence of an escalating global energy crisis and rising pollution levels significantly hampers efforts to achieve sustainable development. This underscores the urgent need for cleaner energy sources and technological advancements to mitigate carbon emissions and reduce air pollution [4,5]. In response to these growing demands, the quest for renewable energy alternatives has brought silicon-based solar cells to the forefront as a promising and viable solution [6]. Research into alternative photovoltaic materials is gaining momentum due to the challenges associated with the production complexity and relatively low conversion efficiency of silicon-based solar cells [7,8]. As the global drive for green energy accelerates, hydrogen is emerging as a highly promising alternative due to its abundant supply, superior energy density, and potential for producing carbon-free energy [6,9]. With current annual hydrogen consumption at 70 million tons, projections suggest a 70% increase in global demand by 2050 [10]. Despite its promise as a clean energy carrier, hydrogen's widespread adoption is hindered by the challenges related to establishing safe, efficient, and economically viable storage and distribution systems [11]. Traditional hydrogen storage methods, such as high-pressure compression and cryogenic liquefaction, are plagued by high costs and significant safety risks. In contrast, metal hydrides are garnering increasing interest as a viable alternative due to their high hydrogen storage capacity, reversibility, and favorable reactivity properties [12].

Among the various methods, solid-state hydrogen storage is gaining recognition as a highly viable, efficient, and secure approach for long-term energy storage solutions [13]. Storage systems for hydrogen typically rely on a range of substances, including alloys and hydrides of metals [14,15], layered two-dimensional materials [16], and highly

* corresponding authors at: Department of Physics, Faculty of Science, University of M'sila, 28000 M'sila, Algeria.
E-mail addresses: torkia.ghellab@univ-msila.dz (T. Ghellab), hakim.baaziz@univ-msila.dz (H. Baaziz).

https://doi.org/10.1016/j.comptc.2026.115663
Received 10 November 2025; Received in revised form 20 December 2025; Accepted 7 January 2026
Available online 11 January 2026

porous frameworks that facilitate efficient gas storage. Notable examples include carbon-based nanostructures, organic-inorganic hybrid materials [17,18], and conductive ceramic structures [18,19].

Additionally, liquid organic hydrogen carriers play a key role in the process [20]. Metal hydrides, which store hydrogen at lower pressures, provide higher volumetric energy densities and contribute to increased safety [21]. Hydride perovskites, with their exceptional structural stability, have captured significant attention due to their promising attributes [22–25]. Moreover, the stability of these materials can be further enhanced, and desorption temperatures lowered, by introducing metal vacancies or doping with transition metals [26]. Consequently, perovskite-type hydrides are emerging as promising candidates for hydrogen storage, thanks to their low molecular weight, high gravimetric hydrogen density, and optimal desorption conditions.

In recent years, the interest in these materials has significantly risen, as evidenced by a substantial increase in both theoretical and experimental studies [27–29]. A diverse array of metal hydrides has been thoroughly explored for various technological applications, which are typically categorized into two principal types: complex multi-hydrides and simpler binary hydrides. The latter group includes compounds like lithium hydride (LiH_2), magnesium hydride (MgH_2), and calcium hydride (CaH_2) [30,31], which are known for their distinct hydrogen storage properties and potential for energy-related applications.

Extensive research has been conducted on different multi-hydrides, with specific factors, such as the nature of their components, playing a key role in determining their properties. For instance, $LiBH_4$ and $NaAlH_4$ have emerged as promising candidates for solid-state hydrogen storage [32–34]. Furthermore, perovskite materials, renowned for their potential in photovoltaic and optoelectronic technologies, are being increasingly investigated for their efficacy in solid hydrogen storage when integrated with metal hydrides. Wu et al. [35] investigated the structural stability and dynamic behavior of $NaMgH_3$, revealing that its perovskite crystal structure could enhance hydrogenation kinetics. This insight may contribute to the development of novel alloy-based hydrides with superior hydrogen storage capabilities. These materials are regarded as promising candidates for efficient hydrogen storage solutions.

Research has demonstrated that doping strategies can significantly improve the hydrogen storage capacities of these materials. For instance, the doped compound $LiCaF_{3-\alpha}H_\alpha$ (where $\alpha = 0, 1, 2, 3$), studied using CASTEP, showed notable enhancements in both gravimetric and volumetric hydrogen storage, achieving up to 6.04 wt%, meeting the U. S. Department of Energy's (DOE) 2050 target [36]. Additionally, a computational study by Xiao et al. [37] on $Li_xNa_{1-x}MgH_3$ ($x = 0$, 0.25, 0.5, 0.75), using VASP, revealed that increasing Li substitution enhanced thermodynamic stability, along with a near-linear decrease in dehydrogenation enthalpies for certain pathways, indicating beneficial modifications for hydrogen storage. In another study, Chami et al. [12] employed WIEN2K to examine $Na_{1-x}K_xMgH_3$ ($x = 0$, 0.25, 0.5, 0.75) and found that the hydrogen storage capacities were 5.67, 5.56, 5.18, and 4.85 wt%, respectively. Supporting these findings, Tao et al. [38] demonstrated experimentally that incorporating potassium instead of sodium improved the dehydriding capabilities of $NaMgH_3$.

Extensive prior research has highlighted the potential of $BaLiH_3$ and $SrLiH_3$ as candidates for hydrogen storage applications. Ghebouli et al. [39] conducted a detailed investigation into the structural, elastic, electronic, and optical properties of these materials under varying pressure conditions, revealing key insights into their behavior and suitability for hydrogen storage. In a similar vein, Bahloul et al. [40] examined how changes in composition affect the elastic constants and thermophysical properties, such as the Debye temperature and melting point, for the $Sr_{1-x}Ba_xLiH_3$ perovskite series under ambient pressure. Their findings suggest that these compounds hold considerable promise for hydrogen storage, offering potential advantages in energy storage systems. Despite this, uncertainties regarding the stability of these hydrides during experimental synthesis remain, and, as of now, there is a notable absence of experimental data concerning their physical and gravimetric hydrogen storage capacities.

This study aims to investigate the dynamic stability and properties of novel tetragonal $Sr_{1-x}Ba_xLiH_3$ alloys (where x ranges from 0 to 1 in increments of 0.125) through ab-initio computational methods. The primary objective is to contribute to the development of sustainable and reliable hydrogen storage compounds, supporting the broader goal of advancing hydrogen-powered technologies for a greener energy future. This article provides a thorough analysis of the $Sr_{1-x}Ba_xLiH_3$ ($x = 0$, 0.125, 0.25, 0.375, 0.5, 0.625, 0.75, 0.875, 1) alloys, offering an in-depth exploration of their potential as hydrogen storage materials. The outcomes of the simulations were thoroughly analyzed, yielding significant information on the structural and electronic properties of the alloys. These findings emphasize the alloys' potential to serve as promising candidates for hydrogen storage in solid-state systems, due to their favorable characteristics that could enhance storage efficiency and stability.

2. Details of computation

First-principles calculations were employed to systematically investigate the structural and electronic properties of the perovskite hydride alloy $Sr_{1-x}Ba_xLiH_3$ ($x = 0$, 0.125, 0.25, 0.375, 0.5, 0.625, 0.75, 0.875, 1) using the Full Potential Linearized Augmented Plane Wave (FP-LAPW) method implemented in the WIEN2k code [41]. The exchange-correlation energy E_{xc} was approximated using three different functionals: The Local Density Approximation (LDA) [42] and the Generalized Gradient Approximation (GGA) [43], and the Modified Becke-Johnson (mBJ) functional [44], which has become the standard for high-accuracy electronic property predictions. The mBJ functional is particularly effective in improving band gap predictions, providing better agreement with experimental results compared to the LDA/GGA approximations [45,46].

For the computational setup, a cutoff parameter of $k_{max} \times RMT = 9$ was used, where RMT is the Muffin-Tin sphere radius and k_{max} is the magnitude of the largest k-vector in the plane wave expansion. The chosen RMT values were 2.5, 2.3, 2.0, and 1.2 Bohr for Ba, Sr, Li, and H, respectively. The charge density was expanded using Fourier analysis up to $G_{max} = 16$ $(Ryd)^{1/2}$ for the alloy system, and $G_{max} = 12$ $(Ryd)^{1/2}$ for the parent compounds $BaLiH_3$ and $SrLiH_3$. The valence wave functions inside the Muffin-Tin spheres were expanded to a maximum angular momentum of $l_{max} = 10$.

To ensure computational accuracy, a core-valence separation energy of −6.0 Ry was applied. Self-consistency in total energy calculations was achieved with a convergence criterion of 10^{-4} Ryd. A $9 \times 9 \times 9$ k-point mesh was utilized to sample the Brillouin zone (BZ) for adequate precision. Finally, the total energy as a function of the unit cell volume was fitted to the Murnaghan equation of state (EOS) [47], which provided the necessary equation of state parameters for evaluating the structural stability and mechanical properties of the alloys.

3. Results and discussion

3.1. Structural properties of $Sr_{1-x}Ba_xLiH_3$

To evaluate the suitability of materials for hydrogen storage and related energy technologies, a thorough investigation of their intrinsic structural properties is imperative. In this work, we employ first-principles calculations to systematically explore the structural evolution of the inverse perovskite alloy system $Sr_{1-x}Ba_xLiH_3$ across the complete compositional range ($x = 0$, 0.125, 0.25, 0.375, 0.5, 0.625, 0.75, 0.875, 1). A strategic substitutional approach within expanded supercells is used to precisely control the Ba concentration, enabling a detailed study of how varying the Sr/Ba ratio affects the material's lattice geometry, phase stability, and underlying bonding characteristics.

The structural stability and bonding characteristics of each alloy configuration were thoroughly examined through full atomic relaxation

simulations, ensuring that all the alloys reached their most stable configurations. Structural optimizations were carried out for each alloy using both the LDA and the GGA for the exchange-correlation functional. This dual approach was employed to assess the sensitivity of the system's properties to different approximations, ensuring the robustness and accuracy of the results. The final optimized atomic positions for each composition and structural phase, reflecting the fully relaxed configurations, are provided in Table 1.

The structural ground states of the parent compounds, $SrLiH_3$ and $BaLiH_3$, were first determined through full atomic relaxation using density functional theory (DFT) with both GGA and LDA approximations. These calculations converged to an ideal cubic structure characterized by the space group $Pm\bar{3}m$ (No. 221). This assignment is supported by the optimized high-symmetry atomic positions, which correspond to the Wyckoff sites of this space group: the larger cation (Sr^{2+} or Ba^{2+}) resides at the 1a site (0,0,0), the Li^{+} cation at the 1b site (0.5, 0.5, 0.5), and the H^{-} anions at the 3c site (0.5, 0, 0.5). The calculated lattice parameters—3.7537 Å for $SrLiH_3$ and 3.9388 Å for $BaLiH_3$ using GGA—show excellent agreement with available experimental data [48] and established theoretical references [51–53] (see Table 2), confirming $Pm\bar{3}m$as the stable equilibrium structure for the parent compounds.

This configuration defines an inverse perovskite structure. In a conventional perovskite (ABX_3), the larger 'A' cation occupies the cuboctahedral site, while the smaller 'B' cation resides at the center of an anion octahedron. Here, this arrangement is reversed: the small Li^{+} cation occupies the octahedral site at the unit cell center, forming corner-sharing LiH_6 octahedra. Conversely, the larger Sr^{2+} or Ba^{2+} cations occupy the cuboctahedral interstices, each coordinated by twelve H^{-} anions to form SrH_{12} or BaH_{12} polyhedra. This inversion is stabilized by the geometric compatibility between the large ionic radii of Sr^{2+} (1.26 Å) and Ba^{2+} (1.42 Å) and the spacious cuboctahedral site.

To thoroughly examine the impact of barium (Ba) substitution on the structural and electronic properties of the $SrLiH_3$ alloy, we employed a strategic substitution method within expanded supercells. Initially, we utilized a 2 × 2 × 1 supercell to model the $SrLiH_3$ structure, which consists of a unit cell containing four strontium (Sr) atoms. In this configuration, we systematically substituted one, two, three, and four of the Sr cation sites with Ba atoms, achieving alloy compositions with x values of 0.25, 0.5, 0.75, and 1, respectively. For intermediate alloy compositions with x values of 0.125, 0.375, 0.625, and 0.875, we introduced Ba atoms at one, three, five, and seven Sr cation sites within a larger 2 × 2 × 2 supercell, containing a total of eight Sr atoms. This substitution approach allows for a precise control of Ba concentration, providing a diverse range of alloy compositions for a comprehensive study. By exploring these variations, we can investigate how changes in Ba content affect the material's structural stability, electronic behavior, and potential for hydrogen storage applications. This method not only sheds light on the effects of cation substitution but also lays the groundwork for designing optimized materials for energy storage systems. This methodology, which systematically adjusts the concentration of Ba in the alloy, provides a comprehensive means to study the structural and electronic changes induced by varying the Sr/Ba ratio. The resulting alloys offer a rich platform for understanding the influence of cation substitution on the material's hydrogen storage properties, as well as its stability, electronic behavior, and potential for practical applications in energy systems.

The evolution of the unit cells in $Sr_{1-x}Ba_xLiH_3$ ($x = 0$, 0.125, 0.25, 0.375, 0.5, 0.625, 0.75, 0.875, 1) alloys, as illustrated in Fig. 1, demonstrates a complex interplay between composition, symmetry, and local coordination environments. At $x = 0$ ($SrLiH_3$), the structure crystallizes in the cubic space group $Pm\bar{3}m$ (No. 221), characterized by a three-dimensional network of corner-sharing LiH_6 octahedra, with Sr^{2+} ions occupying the cuboctahedral interstices to form SrH_{12} units. This arrangement reflects the geometric flexibility of the perovskite-like

Table 1
Calculated atomic positions of $Sr_{1-x}Ba_xLiH_3$ ($x = 0$, 0.125, 0.25, 0.375, 0.5, 0.625, 0.75, 0.875, 1) alloys using the GGA and LDA approximations.

Alloys	*Atomic positions*	
	GGA	**LDA**
$SrLiH_3$ ($Pm\bar{3}m$)	**Sr (0.0, 0.0, 0.0)** **Li (0.5, 0.5, 0.5)** **H (0.5, 0.0, 0.5)**	**Sr (0.0, 0.0, 0.0)** **Li (0.5, 0.5, 0.5)** **H (0.5, 0.0, 0.5)**
$Ba_{0.125}Sr_{0.875}LiH_3$ ($Pm\bar{3}m$)	**Ba1 (0.0, 0.0, 0.0)** **Sr1 (0.5, 0.0, 0.0)** **Sr2 (0.5, 0.5, 0.0)** **Sr3 (0.5, 0.5, 0.5)** **Li1 (0.2508, 0.2508, 0.2508)** **H1 (0.2512, 0.0, 0.2512)** **H2 (0.5, 0.2502, 0.2502)**	**Ba1 (0.0, 0.0, 0.0)** **Sr1 (0.5, 0.0, 0.0)** **Sr2 (0.5, 0.5, 0.0)** **Sr3 (0.5, 0.5, 0.5)** **Li1 (0.2504, 0.2504, 0.2504)** **H1 (0.2506, 0.0, 0.2506)** **H2 (0.5, 0.2501, 0.2501)**
$Ba_{0.25}Sr_{0.75}LiH_3$ (*P4/mmm*)	**Ba (0.0, 0.0, 0.0)** **Sr1 (0.5, 0.0, 0.0)** **Sr2 (0.5, 0.5, 0.0)** **Sr3 (0.5, 0.5, 0.5)** **Li (0.2508, 0.2508, 0.2508)** **H1 (0.2512, 0.0, 0.2512)** **H2 (0.5, 0.2502, 0.2502)**	**Ba (0.0, 0.0, 0.0)** **Sr1 (0.5, 0.0, 0.0)** **Sr2 (0.5, 0.5, 0.0)** **Sr3 (0.5, 0.5, 0.5)** **Li (0.2504, 0.2504, 0.2504)** **H1 (0.2506, 0.0, 0.2506)** **H2 (0.5, 0.2501, 0.2501)**
$Ba_{0.375}Sr_{0.625}LiH_3$ (*P4/mmm*)	**Ba1 (0.0, 0.0, 0.0)** **Ba2 (0.5, 0.0, 0.0)** **Sr1 (0.5, 0.5, 0.0)** **Sr2 (0.0, 0.0, 0.5)** **Sr3 (0.5, 0.0, 0.5)** **Sr4 (0.5, 0.5, 0.5)** **Li1 (0.2506, 0.2506, 0.2519)** **H1 (0.2501, 0.0, 0.2522)** **H2 (0.2511,0.2511, 0.0)** **H3 (0.5, 0.2509, 0.2513)** **H4 (0.2502, 0.2502, 0.5)**	**Ba1 (0.0, 0.0, 0.0)** **Ba2 (0.5, 0.0, 0.0)** **Sr1 (0.5, 0.5, 0.0)** **Sr2 (0.0, 0.0, 0.5)** **Sr3 (0.5, 0.0, 0.5)** **Sr4 (0.5, 0.5, 0.5)** **Li1 (0.2506, 0.2506, 0.2519** **H1 (0.2501, 0.0, 0.2523)** **H2 (0.2511, 0.2511, 0.0)** **H3 (0.5, 0.2509, 0.2513)** **H4 (0.2502, 0.2502, 0.5)**
$Ba_{0.5}Sr_{0.5}LiH_3$ (*P4/mmm*)	**Ba1 (0.0, 0.0, 0.0)** **Sr1 (0.0, 0.0, 0.5)** **Li (0.5, 0.5, 0.2532)** **H1 (0.5, 0.0, 0.2531)** **H2 (0.5, 0.5, 0.0)** **H3 (0.5, 0.5, 0.5)**	**Ba1 (0.0, 0.0, 0.0)** **Sr1 ((0.0, 0.0, 0.5)** **Li (0.5, 0.5, 0.2532)** **H1 (0.5, 0.0, 0.2531)** **H2 (0.5, 0.5, 0.0)** **H3 (0.5, 0.5, 0.5)**
$Ba_{0.625}Sr_{0.375}LiH_3$ (*P4/mmm*)	**Ba1 (0.0, 0.0, 0.0)** **Ba2 (0.5, 0.0, 0.0)** **Ba3 (0.5, 0.5, 0.0)** **Ba4 (0.0, 0.0, 0.5)** **Sr1 (0.5, 0.0, 0.5)** **Sr2 (0.5, 0.5, 0.5)** **Li (0.2506, 0.2506, 0.2518)** **H1 (0.2511, 0.0, 0.2514)** **H2 (0.2501, 0.2501, 0.0)** **H3 (0.5, 0.2502, 0.2522)** **H4 (0.2509, 0.2509, 0.5)**	**Ba1 (0.0, 0.0, 0.0)** **Ba2 (0.5, 0.0, 0.0)** **Ba3 (0.5, 0.5, 0.0)** **Ba4 (0.0, 0.0, 0.5)** **Sr1 (0.5, 0.0, 0.5)** **Sr2 (0.5, 0.5, 0.5)** **Li (0.2506, 0.2506, 0.2519)** **H1 (0.2511, 0.0, 0.2514)** **H2 (0.2501, 0.2501, 0.0)** **H3 (0.5, 0.2502, 0.2523)** **1H4 (0.2509, 0.2509, 0.5)**
$Ba_{0.75}Sr_{0.25}LiH_3$ (*P4/mmm*)	**Ba1 (0.0, 0.0, 0.0)** **Ba2 (0.5, 0.0, 0.0)** **Sr1 (0.5, 0.5, 0.0)** **Li (0.2508, 0.2508, 0.5)** **H1 (0.0, 0.2501, 0.5)** **H2 (0.2507, 0.2507, 0.0)** **H3 (0.5, 0.2510, 0.5)**	**Ba1 (0.0, 0.0, 0.0)** **Ba2 (0.5, 0.0, 0.0)** **Sr1 (0.5, 0.5, 0.0)** **Li1 (0.2508, 0.2508, 0.5)** **H1 (0.0, 0.2501, 0.5)** **H2 (0.2506, 0.2506, 0.0)** **H3 (0.5, 0.2510, 0.5)**
$Ba_{0.875}Sr_{0.125}LiH_3$ ($Pm\bar{3}m$)	**Ba1 (0.0, 0.0)** **Ba2 (0.5, 0.0, 0.0)**	**Ba1 (0.0, 0.0)** **Ba2 (0.5, 0.0, 0.0)**

(*continued on next page*)

Table 1 (*continued*)

Alloys	*Atomic positions*	
	GGA	**LDA**
$BaLiH_3$ (***Pm$\bar{3}$m***)	**Ba3 (0.5, 0.5, 0.0)** **Sr1 (0.5, 0.5, 0.5)** **Li1 (0.25, 0.25, 0.25)** **H1 (0.25, 0.0,0.25)** **H2 (0.5, 0.25, 0.25)** **Ba (0.0, 0.0, 0.0)** **Li (0.5, 0.5, 0.5)** **H (0.5, 0.0, 0.5)**	**Ba3 (0.5, 0.5, 0.0)** **Sr1 (0.5, 0.5, 0.5)** **Li1 (0.25, 0.25, 0.25)** **H1 (0.25, 0.0, 0.25)** **H2 (0.5, 0.25, 0.25)** **Ba (0.0, 0.0, 0.0)** **Li (0.5, 0.5, 0.5)** **H (0.5, 0.0, 0.5)**

framework, where the larger Sr^{2+} cations (in 12-coordination) stabilize the lattice through high hydrogen coordination, while the distorted linear H^- geometry mediates ionic bonding between Li^+ and Sr^{2+}.

Upon initial Ba substitution ($x = 0.125$), the cubic symmetry persists, indicating that the lattice can accommodate the slightly larger Ba^{2+} ions without significant distortion. This suggests a homogeneous solid-solution regime at low Ba concentrations, where statistical occupancy of Sr and Ba in the cuboctahedral sites minimally perturbs the LiH_6 network. However, as the Ba content increases (x = 0.25–0.75), the system undergoes a cubic-to-tetragonal (*P4/mmm*) transition, driven by increasing lattice strain from the size disparity between Sr^{2+} and Ba^{2+}. The tetragonal distortion reflects a compromise between the geometric constraints of the LiH_6 octahedra and the cuboctahedral Sr/BaH_{12} sites, with the latter exhibiting elongated bond lengths along one axis to mitigate steric repulsion. This intermediate phase highlights the role of elastic anisotropy in accommodating larger cations, where the hydrogen sublattice adapts through bond-length and angular adjustments to preserve connectivity.

Notably, at $x = 0.875$, the structure reverts to cubic symmetry (*Pm$\bar{3}$m*), though with expanded lattice parameters compared to the x = 0 phase. This reentrant cubic behavior implies a threshold concentration effect, where the Ba-rich environment stabilizes a new equilibrium in cuboctahedral packing, possibly due to reduced strain heterogeneity or a shift in hydrogen coordination preferences. For $x = 1$ ($BaLiH_3$), the structure adopts the *Pm$\bar{3}$m* (No. 221) space group, distinct from the Sr analog, with face-sharing LiH_6 octahedra and BaH_{12} cuboctahedra. This rearrangement underscores the compositional dependence of polyhedral connectivity: while $SrLiH_3$ favors corner-sharing for optimal Sr—H distances, $BaLiH_3$ maximizes space-filling efficiency through face-sharing, likely due to Ba^{2+}'s larger polarizability and weaker directional bonding with H^-.

The persistence of distorted linear H^- geometries across all compositions suggests a robust ionic-covalent bonding framework, where H^- acts as a bridging ligand between Li^+ and Sr^{2+}/Ba^{2+}. However, the bond-angle variability in the tetragonal phase hints at dynamic adjustments in hydrogen positions to balance steric and electronic effects. Comparatively, the phase transitions mirror trends in perovskite oxides, where A-site cation size variance often drives symmetry lowering (e.g., cubic-tetragonal-orthorhombic). Here, the re-stabilization of cubic symmetry at high x deviates from classical Vegard's law behavior, implying additional factors such as hydrogen-mediated screening or entropic contributions at elevated Ba concentrations.

Further investigation is warranted to resolve whether the $x = 0.875$ cubic phase exhibits short-range cation ordering or dynamic disorder, as well as the potential impact of hydrogen vibrational entropy on phase stability. Additionally, the electronic structure evolution—particularly the Li—H and Ba/Sr-H bonding interactions-could elucidate the interplay between geometric distortion and properties such as hydride mobility or optoelectronic response.

First-principles calculations were systematically employed to investigate the structural properties of $Sr_{1-x}Ba_xLiH_3$ across the complete compositional range (x = 0 to 1). The Murnaghan equation of state [47] was fitted to energy-volume data, yielding characteristic parabolic

Table 2
Calculated values of Structural Parameters for $Sr_{1-x}Ba_xLiH_3$ alloys (x = 0–1).

Alloys	Structural parameters	GGA	LDA
$SrLiH_3$ (***Pm$\bar{3}$m***)	***a* (Å)**	**3.7537,** 3.8044[a], 3.8044 [b], 3.788[c], 3.833[e], 3.81[f]	**3.7017**, 3.7026[a], 3.696[c]
	Relative error in a	$\left.\frac{\Delta a}{a}\right\|_{exp}$ = ***2.11***%	$\left.\frac{\Delta a}{a}\right\|_{exp}$ = ***3.54***%
	V(Å^3)	**52.8906,** 55.138[d]	**50.7228**
	B(GPa)	**45.7690,** 42.955[a], 42.8[b], 40.729[d]	**50.7228,** 50.625[c]
	B′	**3.7079,** 3.805[a], 3.834[d]	**3.6831**, 3.721[c]
	E_0(Ryd)	**−6374.455080**	**−6370.855387**
$Ba_{0.125}Sr_{0.875}LiH_3$ (***Pm$\bar{3}$m***)	***a* (Å)**	**3.7825**	**3.7289**
	V(Å^3)	**54.1173**	**51.8492**
	B(GPa)	**45.0141**	**49.7917**
	B′	**3.5022**	**3.7002**
	E_0 (Ryd)	**−7614.0136**	**−7610.0906**
$Ba_{0.25}Sr_{0.75}LiH_3$ (*P4/mmm*)	***a* (Å)**	**3.7931**	**3.7478**
	***c* (Å)**	**3.8048**	**3.7542**
	c/a	**0.9969**	**0.9982**
	V(Å^3)	**54.7419**	**52.7315**
	B(GPa)	**44.4004**	**48.8271**
	B′	**3.6300**	**3.5724**
	E_0 (Ryd)	**−8853.5739**	**−8849.3265**
$Ba_{0.375}Sr_{0.625}LiH_3$ (*P4/mmm*)	***a* (Å)**	**3.8286**	**3.7788**
	***c* (Å)**	**3.8555**	**3.7843**
	c/a	**1.0070**	**1.0014**
	V(Å^3)	**56.5146**	**54.0372**
	B(GPa)	**43.7793**	**48.3073**
	B′	**3.7605**	**3.6988**
	E_0 (Ryd)	**−10,093.1340**	**−10,088.5629**
$Ba_{0.5}Sr_{0.5}LiH_3$ (*P4/mmm*)	***a* (Å)**	**3.8528,** 3.9276[a]	**3.8016,** 3.8245[a]
	***c* (Å)**	**3.8583**	**3.807**
	c/a	**1.0014**	**1.0014**
	V(Å^3)	**57.2728**	**55.0193**
	B(GPa)	**43.0197,** 39.718[a]	**47.8547,** 47.074[a]
	B′	**2.4231,** 3.789[a]	**3.8416,** 3.856[a]
	E_0 (Ryd)	**−11,332.6947**	**−11,327.7999**
$Ba_{0.625}Sr_{0.375}LiH_3$ (*P4/mmm*)	***a* (Å)**	**3.8746**	**3.8272**
	***c* (Å)**	**3.8823**	**3.8377**
	c/a	**1.0019**	**1.0027**
	V(Å^3)	**58.2831**	**56.2125**
	B(GPa)	**42.7004**	**46.9436**
	B′	**3.7110**	**3.9421**
	E_0 (Ryd)	**−12,572.2550**	**−12,567.0362**
$Ba_{0.75}Sr_{0.25}LiH_3$ (*P4/mmm*)	***a* (Å)**	**3.8894**	**3.8440**
	***c* (Å)**	**3.8969**	**3.8489**
	c/a	**0.9980**	**0.9987**
	V(Å^3)	**58.9500**	**56.8726**
	B(GPa)	**42.1519**	**46.2228**
	B′	**3.7265**	**3.7675**
	E_0 (Ryd)	**−13,811.8158**	**−13,806.2737**
$Ba_{0.875}Sr_{0.125}LiH_3$ (***Pm$\bar{3}$m***)	***a* (Å)**	**3.9184**	**3.8708**
	V(Å^3)	**60.0102**	**57.985**
	B(GPa)	**41.6342**	**45.7411**
	B′	**3.6783**	**3.7244**
	E_0 (Ryd)	**−15,051.3771**	**−15,045.5114**
$BaLiH_3$ (***Pm$\bar{3}$m***)	***a* (Å)**	**3.9388,** 4.0003[a], 4.0148[b], 3.989[c],4.010[d], 4.023[e], 4.005[f]	**3.8915,** 3.8930[a], 3.892[c]
	Relative error in a	$\left.\frac{\Delta a}{a}\right\|_{exp}$ = ***2.13***%	$\left.\frac{\Delta a}{a}\right\|_{exp}$ = ***3.37***%
	V(Å^3)	**60.1625,** 64.506[d]	**58.9319**
	B(GPa)	**40.2966,** 37.953[a], 40.141[d], 38.2[b]	**45.4941,** 45.916[c]
	B′	**3.9595,** 3.654[a], 3.902[d]	**3.6528,** 3.848[c]
	E_0 (Ryd)	**−16,290.9388**	**−16,284.7495**

[a] *PP-GGA/LDA* [40], [b]*PP-GGA* [49], [c]*PP-GGA/LDA* [39], [d]*PP-GGA* [50], [e]Experimental data of Ref [48], [f]*FP-GGA* [51].

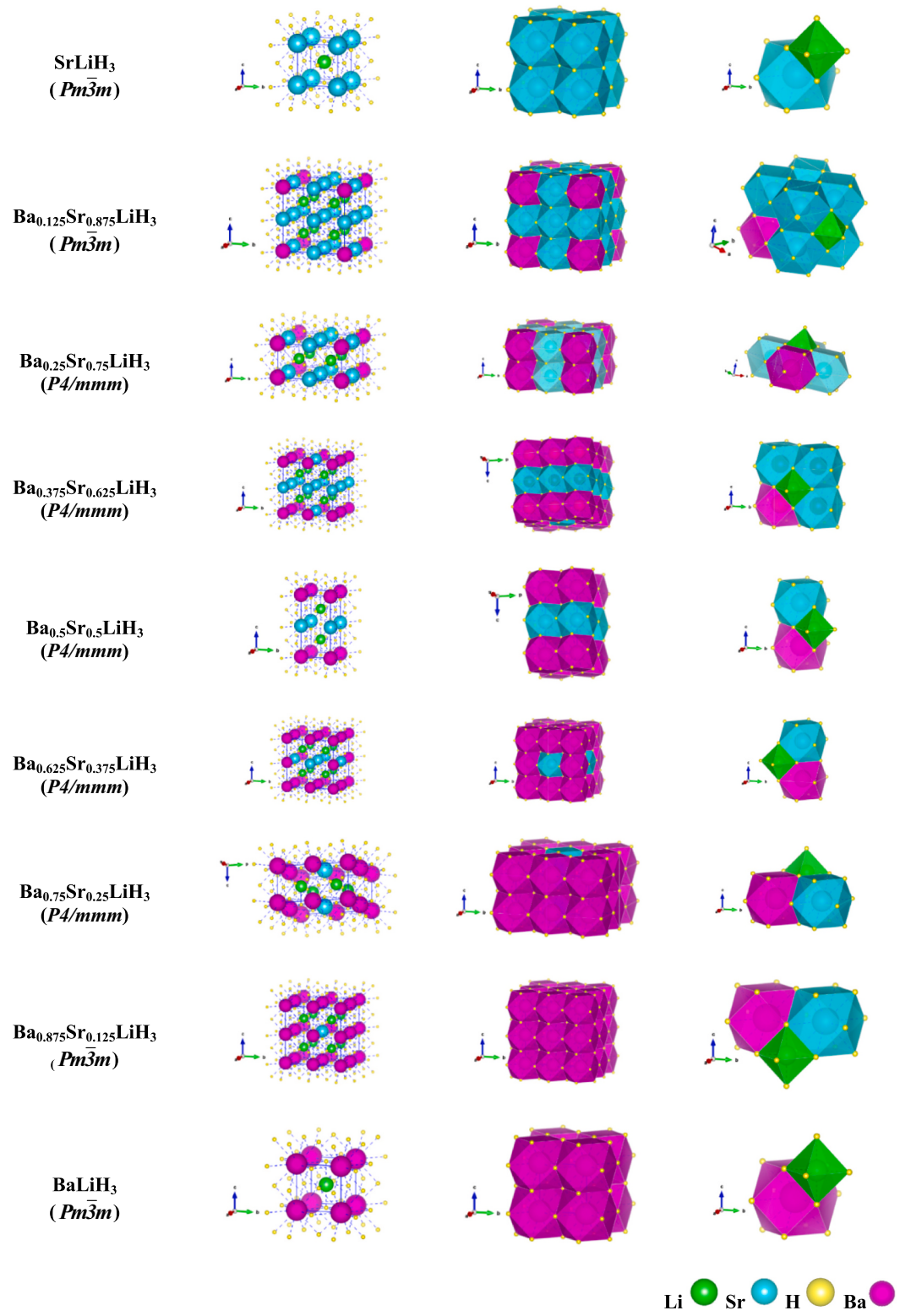

Fig. 1. The different structural phases of $Sr_{1-x}Ba_xLiH_3$ (x = 0, 0.125, 0.25, 0.375, 0.5, 0.625, 0.75, 0.875, 1).

curves that demonstrate the influence of exchange-correlation functionals on ground-state properties (Fig. 2(a)). Each composition exhibits a distinct energy minimum at its equilibrium volume (V_0), providing the basis for deriving fundamental structural and mechanical parameters. The calculated lattice parameters, equilibrium volumes, bulk moduli (B), and their pressure derivatives (B') and minimum total energy (E_0) are presented in Table 2 reveal clear compositional trends, including a 13.75% volumetric expansion from $x = 0$ to $x = 1$ and a corresponding 11.96% reduction in bulk modulus, consistent with the larger ionic radius of Ba^{2+} (1.42 Å) compared to Sr^{2+} (1.26 Å).

The reliability of our computational approach was validated through comprehensive comparisons with experimental and theoretical data. For $SrLiH_3$ ($x = 0$), the GGA-calculated lattice parameter (a = 3.7537 Å) shows excellent agreement with experimental data (3.833 Å [48]), with

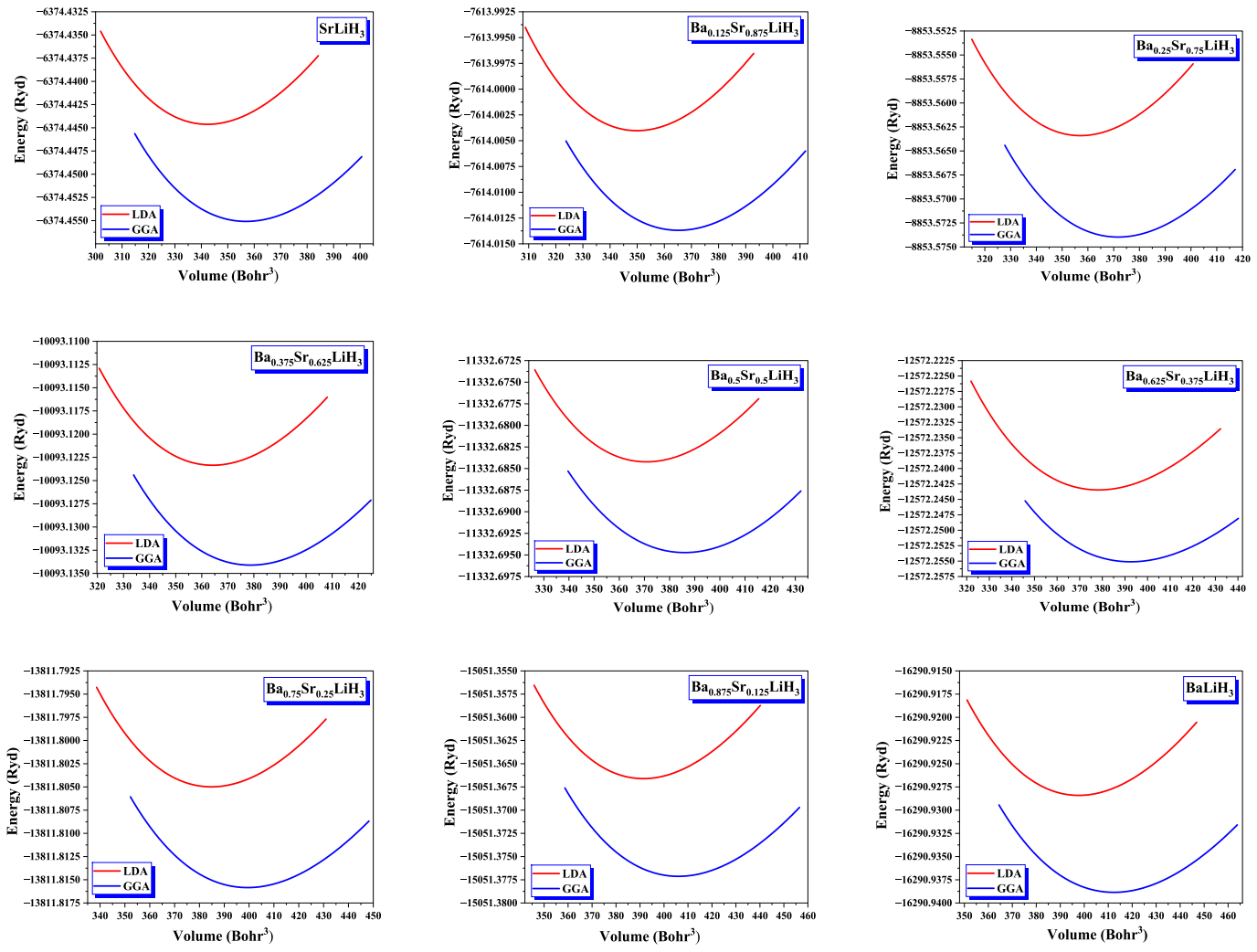

(a)

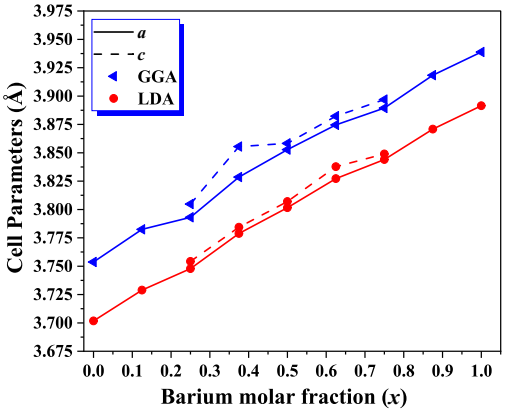

(b)

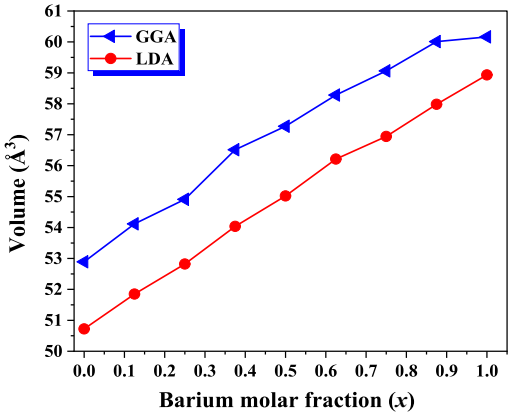

(c)

Fig. 2. (a) Total energy-volume relations and the derived (b) equilibrium lattice constants and (c) unit cell volumes for $Sr_{1-x}Ba_xLiH_3$ (x = 0 to 1), calculated using GGA and LDA.

a minimal 2.11% error, while the LDA result (3.7017 Å) exhibits a slightly larger 3.42% deviation. Similar precision is observed for $BaLiH_3$ ($x = 1$), where the GGA value (3.9388 Å) compares favorably with both experimental (4.023 Å [48], 2.09% error) and theoretical (4.005 Å [51], 1.65% deviation) references. Intermediate compositions, such as $Ba_{0.5}Sr_{0.5}LiH_3$ ($x = 0.5$), show comparable agreement, with GGA predicting $a = 3.8528$ Å versus theoretical values of 3.8245 Å [40].

Volume calculations demonstrate systematic expansion from 52.8906 $Å^3$ (GGA, $x = 0$) to 60.1625 $Å^3$ (GGA, $x = 1$), though with somewhat larger discrepancies compared to theoretical references (e.g., 6.73% underestimation versus Shah's 64.506 $Å^3$ [50] at $x = 1$). This reflects the inherent challenges in modeling hydrogen-related packing effects. The LDA consistently predicts smaller volumes (3–5% lower than GGA), such as 50.7228 $Å^3$ versus 52.8906 $Å^3$ at $x = 0$, due to its characteristic over binding tendency.

Mechanical properties exhibit equally significant trends, with the bulk modulus decreasing from 45.7690 GPa ($x = 0$) to 40.2966 GPa ($x = 1$) under GGA, indicating progressive lattice softening with Ba incorporation. This mechanical response correlates directly with the volumetric expansion and suggests diminished structural stability at higher Ba concentrations. The pressure derivative B' remains remarkably consistent (2–4 range) across all compositions, demonstrating moderate anharmonicity under compression.

The comparative performance of GGA and LDA follows established theoretical expectations, with GGA generally providing better agreement with experimental lattice parameters (<3% error versus LDA's 3–4%), while both approximations show larger deviations (4–9%) in volume predictions. These systematic variations highlight the importance of functional choice in theoretical predictions of complex hydrides.

The compositional dependence of lattice parameters and unit cell volumes in $Sr_{1-x}Ba_xLiH_3$ ($x = 0$, 0.125, 0.25, 0.375, 0.5, 0.625, 0.75, 0.875, 1) (Fig. 2(b) and (c)) reveals fundamental structural trends governed by ionic size effects. The lattice constants (Fig. 2(b)) exhibit near-linear expansion from 3.7537 Å ($x = 0$) to 3.9388 Å ($x = 1$) under GGA, with LDA showing parallel but offset behavior (3.7017 Å to 3.8915 Å). This 5.0% increase in lattice parameters corresponds to the larger ionic radius of Ba^{2+} compared to Sr^{2+}, where the GGA-LDA divergence (1.4–1.7% across the series) reflects their characteristic treatment of electron exchange-correlation. Volumetric expansion (Fig. 2(c)) displays stronger nonlinearity, with GGA predicting 13.8% growth (52.8906 $Å^3$ to 60.1625 $Å^3$) versus LDA's 16.2% (50.7228 $Å^3$ to 58.9319 $Å^3$). The curvature suggests progressive accumulation of lattice strain, particularly beyond $x = 0.5$, where each additional Ba ion induces greater volumetric distortion than at lower concentrations. The widening GGA-LDA gap at high Ba content (2.1 $Å^3$ difference at $x = 0$ versus 2.6 $Å^3$ at $x = 1$) implies increasing sensitivity to the choice of exchange-correlation functional as the hydride becomes Ba-rich.

Notably, both approximations show continuous evolution without discontinuities, confirming complete solid solubility across the Sr—Ba series. The systematic offset between GGA and LDA trends (3–5% for lattice parameters, 4–6% for volumes) maintains consistent proportionality, demonstrating that while absolute values differ, both methods capture the same underlying physics of size-driven expansion. These structural trends provide the foundation for understanding electronic and mechanical property variations across the compositional range.

The structural evolution of $Sr_{1-x}Ba_xLiH_3$ ($x = 0$, 0.125, 0.25, 0.375, 0.5, 0.625, 0.75, 0.875, 1) across the compositional range reveals systematic trends in bond lengths and polyhedral volumes, as summarized in Table 3, with notable deviations between our DFT results and established theoretical studies. For $SrLiH_3$ ($x = 0$), our GGA calculations (Table 3) yield Sr—H and Li—H bond lengths of 2.6171 Å and 1.8768 Å, respectively, while LDA predicts slightly shorter values of 2.5606 Å and 1.87683 Å. These agree well with literature values, such as the Sr—H (2.71174 Å) and Li—H (1.91749 Å) distances reported by Kunkel et al. [52], as well as the nearly identical results of Orgaz & Gupta (2.711 Å

Table 3
Selected interatomic distances (Å) and angles (deg) in $Sr_{1-x}Ba_xLiH_3$ ($x = 0$–1).

Alloys	Atoms	Approximations	
		GGA	**LDA**
$SrLiH_3$ (***Pm$\bar{3}$m***)	**Sr-H (×12)**	**2.6542,** 2.71174 [52], 2.711 [53]	**2.65424**
	SrH_{12} polyhedral volume	**44.0743 $Å^3$**	**44.0743 $Å^3$**
	Li-H (×6)	**1.8768,** 1.91749 [52], 1.917 [53]	**1.87683**
	LiH_6 polyhedral volume	**8.8149 $Å^3$**	**8.8149 $Å^3$**
$Ba_{0.125}Sr_{0.875}LiH_3$ (***Pm$\bar{3}$m***)	**Ba-H (×12)**	**2.68792**	**2.63802**
	BaH_{12} polyhedral volume	**45.7733 $Å^3$**	**43.2472 $Å^3$**
	Sr-H1 (×8)	**2.67466**	**2.63674**
	Sr-H2 ((×4)	**2.67714**	**2.63802**
	SrH_{12} polyhedral volume	**45.17 $Å^3$**	**43.2472 $Å^3$**
	Li-H1 (×3)	**1.88497**	**1.86121**
	Li-H2 (×3)	**1.89755**	**1.86769**
	LiH_6 polyhedral volume	**9.0194 $Å^3$**	**8.6415 $Å^3$**
$Ba_{0.25}Sr_{0.75}LiH_3$ (*P4/mmm*)	**Ba-H1 (×8)**	**2.69751**	**2.66578**
	Ba-H2 (×4)	**2.70257**	**2.66668**
	BaH_{12} polyhedral volume	**46.3837 $Å^3$**	**44.6992 $Å^3$**
	Sr-H1 (×4)	**2.67512**	**2.64361**
	Sr-H2 (×4)	**2.68847**	**2.65470**
	Sr-H3 (×4)	**2.69043**	**2.65679**
	SrH_{12} polyhedral volume	**45.6365 $Å^3$**	**43.9757 $Å^3$**
	Li-H1 (×2)	**1.89300**	**1.86739**
	Li-H2 (×2)	**1.89659**	**1.87714**
	Li-H3 (×2)	**1.91182**	**1.88690**
	LiH_6 polyhedral volume	**9.1519 $Å^3$**	**8.8190 $Å^3$**
$Ba_{0.375}Sr_{0.625}LiH_3$ (*P4/mmm*)	**Ba-H1 (×4)**	**2.70727**	**2.67206**
	Ba-H2 (×4)	**2.72854**	**2.68564**
	Ba-H3 (×4)	**2.72961**	**2.68674**
	BaH_{12} polyhedral volume	**47.5594 $Å^3$**	**45.4804 $Å^3$**
	Sr-H (×4)	**2.70363**	**2.65975**
	Sr-H2 (×4)	**2.70725**	**2.67609**
	Sr-H3 (×4)	**2.71466**	**2.67609**
	SrH_{12} polyhedral volume	**46.8663 $Å^3$**	**44.8986 $Å^3$**
	Li-H1 (×2)	**1.90940**	**1.88437**
	Li-H2 (×1)	**1.91306**	**1.87706**
	Li-H3 (×2)	**1.91923**	**1.89447**
	Li-H4 (×1)	**1.94252**	**1.90729**
	LiH_6 polyhedral volume	**9.4193 $Å^3$**	**9.0063 $Å^3$**
$Ba_{0.5}Sr_{0.5}LiH_3$ (*P4/mmm*)	**Ba-H1 (×4)**	**2.72436**	**2.68816**
	Ba-H2 (×8)	**2.74382**	**2.70734**
	BaH_{12} polyhedral volume	**48.3388 $Å^3$**	**46.4367 $Å^3$**
	Sr-H1 (×8)	**2.70890**	**2.67288**
	Sr-H2 (×4)	**2.72436**	**2.68816**
	SrH_{12} polyhedral volume	**47.1177 $Å^3$**	**45.2637 $Å^3$**
	Li-H1 (×1)	**1.90370**	**1.87838**
	Li-H2 (×4)	**1.92641**	**1.90082**
	Li-H3 (×1)	**1.95463**	**1.92862**
	LiH_6 polyhedral volume	**9.5457 $Å^3$**	**9.1700 $Å^3$**
$Ba_{0.625}Sr_{0.375}LiH_3$ (*P4/mmm*)	**Ba-H1 (×4)**	**2.73831**	**2.70482**
	Ba-H2 (×8)	**2.75394**	**2.72141**
	BaH_{12} polyhedral volume	**48.9500 $Å^3$**	**47.2154 $Å^3$**
	Sr-H1 (×8)	**2.72877**	**2.69630(**
	Sr-H1 (×4)	**2.72905**	**2.69559**
	SrH_{12} polyhedral volume	**47.9256 $Å^3$**	**46.2183 $Å^3$**
	Li-H1 (×1)	**1.92645**	**1.90369**
	Li-H2 (×2)	**1.93244**	**1.90859**
	Li-H3 (×2)	**1.94215**	**1.91862**

(*continued on next page*)

Table 3 (*continued*)

Alloys	Atoms	Approximations	
		GGA	**LDA**
	Li-H4 (×1)	**1.94215**	**1.93410**
	LiH_6 polyhedral volume	**9.7137 Å^3**	**9.3689 Å^3**
$Ba_{0.75}Sr_{0.25}LiH_3$ (*P4/mmm*)	**Ba-H1 (×4)**	**2.75895**	**2.71737**
	Ba-H2 (×4)	**2.75559**	**2.72164**
	Ba-H2 (×4)	**2.75204**	**2.72416**
	BaH_{12} polyhedral volume	**49.3324 Å^3**	**47.5039 Å^3**
	Sr-H1 (×8)	**2.74688**	**2.71231**
	Sr-H2 (×4)	**2.74786**	**2.71402**
	SrH_{12} polyhedral volume	**48.8848 Å^3**	**47.0750 Å^3**
	Li-H1 (×2)	**1.95512**	**1.91760**
	Li-H2 (×2)	**1.94187**	**1.91967**
	Li-H3 (×2)	**1.94471**	**1.93137**
	LiH_6 polyhedral volume	**9.8444 Å^3**	**9.4796 Å^3**
$Ba_{0.875}Sr_{0.125}LiH_3$ (***Pm$\bar{3}$m***)	**Ba-H (×12)**	**2.77074**	**2.73705**
	BaH_{12} polyhedral volume	**50.1364 Å^3**	**48.3294 Å^3**
	Sr-H (×12)	**2.77074**	**2.73705**
	SrH_{12} polyhedral volume	**50.1364 Å^3**	**48.3294 Å^3**
	Li-H (×6)	**1.95921**	**1.93539**
	LiH_6 polyhedral volume	**10.0273 Å^3**	**9.6659 Å^3**
$BaLiH_3$ (***Pm$\bar{3}$m***)	**Ba-H (×12)**	**2.7851,** 2.84458 [52], 2.845 [53]	**2.75168**
	BaH_{12} polyhedral volume	**50.9235 Å^3**	**49.1085 Å^3**
	Li-H (×6)	**1.9694,** 2.01142 [52], 2.012 [53]	**1.94573**
	LiH_6 polyhedral volume	**10.1847 Å^3**	**9.8217 Å^3**

Sr—H, 1.917 Å Li—H) [53]. The observed deviations of 3.5–4.9% for metal-hydrogen bonds and < 2.1% for Li—H distances (Table 3) highlight the stability of lithium's tetrahedral coordination, which remains remarkably consistent across methodologies.

As Ba substitution increases, the bond length distribution becomes more complex, with detailed values provided in Table 3. At intermediate compositions ($x = 0.5$), Ba—H bonds span 2.72436–2.74382 Å (GGA) and 2.68816–2.70734 Å (LDA), while Sr—H bonds exhibit similar variability (2.70890–2.72436 Å GGA; 2.67288–2.68816 Å LDA). In contrast, Li—H bonds remain relatively stable (1.90370–1.95463 Å GGA; 1.87838–1.92862 Å LDA), as shown in Table 3, with the 5–6% variation within each bond category reflecting local strain induced by Sr/Ba substitution. The persistent 2–3% offset between GGA and LDA values underscores the expected methodological differences, while the minimal distortion of the Li—H geometry demonstrates the structural adaptability of the lithium sublattice. For the $BaLiH_3$ endpoint ($x = 1$), our GGA-calculated bond lengths (2.9498 Å Ba–H; 1.9694 Å Li—H, Table 3) show more significant deviations from reference values (e.g., 2.84458 Å Ba—H and 2.01142 Å Li—H [52]). The 3.6–4.2% overestimation in Ba—H bonds and 2.1–2.3% underestimation in Li—H bonds (Table 3) may arise from increased sensitivity to computational parameters in Ba-rich compositions, unaccounted anharmonic effects, or pseudopotential limitations for barium.

The progression from $x = 0$ to $x = 1$ (Table 3) demonstrates several fundamental trends. The (Sr/Ba)–H bonds expand nonlinearly by 12.7% (GGA) and 11.9% (LDA), while Li—H bonds vary by less than 5% despite the cubic-to-tetragonal symmetry transition. The consistent 2.8–3.1% bond length reduction in LDA compared to GGA across all compositions (Table 3) confirms the expected functional-dependent trends. These comparisons not only validate our computational approach but also identify Ba-rich compositions ($x > 0.75$) as particularly sensitive to computational parameters, suggesting they may require specialized treatment in future studies.

Polyhedral volume analysis (Table 3) provides further insights into the structural accommodation of Ba substitution. The BaH_{12} polyhedra expand by 15.5% (GGA: 44.0743 Å^3 → 50.9235 Å^3), with nonlinear growth most pronounced between $x = 0.25$–0.625 (~1.0 Å^3 per 0.125 Ba increment), coinciding with the cubic-to-tetragonal phase transition. LDA predicts a similar but compressed trend (11.4% increase), consistent with its treatment of electron correlation. In contrast, SrH_{12} polyhedra exhibit anomalous expansion in mixed compositions, reaching 48.8848 Å^3 at x = 0.75 (GGA)—a 10.9% increase over the $x = 0$ value—despite decreasing Sr content (Table 3). This suggests strain accommodation mechanisms where Sr sites expand to mitigate lattice mismatch in the Ba-dominated environment. The volume difference between SrH_{12} and BaH_{12} narrows from 0 Å^3 ($x = 0$) to just 2.0 Å^3 ($x = 0.875$), indicating progressive convergence of their structural roles. Meanwhile, LiH_6 polyhedral expand proportionally to the metal polyhedra (+15.5% GGA, +11.4% LDA, Table 3), maintaining a near-constant volume ratio ($V_{(LiH_6)}/V_{(metalH_{12})} \approx 0.20 \pm 0.01$) across all compositions.

Three key structural implications emerge from these observations (Table 3). First, the BaH_{12} polyhedra dominate the volumetric expansion, with nonlinear growth suggesting critical composition thresholds ($x \approx 0.375$) for lattice rearrangement. Second, the anomalous expansion of SrH_{12} polyhedra reveals unanticipated strain accommodation mechanisms in mixed compositions. Third, the LiH_6 polyhedra exhibit exceptional geometric flexibility, maintaining ideal coordination even as the metal-hydrogen framework undergoes significant distortion. Collectively, these trends demonstrate that while Ba substitution drives volumetric changes through metal-hydrogen bond lengthening, the lithium sublattice provides essential stability across the compositional range.

The structural evolution observed here provides important insights into the potential synthesis pathways for $Sr_{1-x}Ba_xLiH_3$. The continuous solid solubility across the entire composition range, evidenced by the systematic lattice expansion without phase segregation, indicates that homogeneous alloys should be accessible via conventional solid-state methods. A plausible synthesis route would involve high-energy ball milling or direct sintering of stoichiometric mixtures of SrH_2/BaH_2 and LiH under a hydrogen atmosphere, analogous to the preparation of related perovskite hydrides like $NaMgH_3$. The moderate volumetric expansion (13.8% total) and absence of reconstructive phase transitions suggest that diffusion-controlled kinetic barriers may be surmountable at moderate temperatures (≈600–700 K). However, the cubic-to-tetragonal distortion at intermediate compositions ($x = 0.25$–0.75) could introduce anisotropic diffusion pathways that may affect reaction rates. The structural stability of the parent compounds ($SrLiH_3$ and $BaLiH_3$) and the re-entrant cubic phase at $x = 0.875$ should facilitate nucleation and growth. Future computational studies should explicitly calculate cation migration barriers to identify rate-limiting steps and optimize synthesis protocols.

This detailed structural analysis reveals the key mechanisms underpinning hydrogen storage performance. The stability of the LiH_6 octahedra ensures the hydrogen sublattice remains intact during cycling, a prerequisite for reversibility. The expansion of $(Sr/Ba)H_{12}$ polyhedra directly creates larger interstitial sites, which can lower the energetic barrier for hydrogen diffusion. Furthermore, the strain-induced cubic-to-tetragonal transition at intermediate compositions introduces anisotropic lattice distortion. This distortion is hypothesized to create preferential pathways for hydrogen migration, potentially enhancing desorption kinetics—a critical parameter for practical applications that warrants future kinetic studies via methods like the Nudged Elastic Band (NEB) technique.

The structural evolution of $Sr_{1-x}Ba_xLiH_3$ reveals exceptional potential for hydrogen storage through three key mechanisms: (1) The inverse perovskite framework maintains stable Li—H coordination (<5% bond variation) during substantial lattice expansion (15.5% volume increase),

with LiH_6 octahedra preserving their volume ratio ($V_{(LiH_6)}/V_{(metalH_{12})} \approx 0.20 \pm 0.01$) across all compositions. (2) The cubic-to-tetragonal transition at $x = 0.25–0.75$ creates anisotropic strain (5–6% bond length variations) that could potentially lower hydrogen migration barriers through distorted LiH_6 channels (c/a ≈ 1.02), a hypothesis that should be tested with explicit diffusion barrier calculations. (3) Ba-rich domains drive expansion (1.0 $Å^3$ per 0.125Ba) while Sr sites provide strain accommodation (10.9% volume increase at $x = 0.75$), overcoming the typical capacity-stability trade-off.

Electronic effects may further influence performance, with Ba substitution inducing electron delocalization and lattice softening. These changes suggest a possible reduction in hydrogen release barriers, though this requires verification through kinetic studies. The optimal composition window ($x = 0.375–0.625$) balances strain-enhanced kinetics with structural stability, while the re-entrant cubic phase at $x = 0.875$ offers opportunities for defect engineering. With 13.8% total volume expansion matching theoretical capacity predictions and tunable mechanical properties, $Sr_{1-x}Ba_xLiH_3$ emerges as a versatile platform for strain-engineered hydrogen storage, combining perovskite flexibility with precise compositional control.

3.2. Formation energy and desorption temperature

The primary objective of these computational investigations is to determine the thermodynamically preferred dehydrogenation pathway. Similar to other ternary metal hydrides, $Sr_{1-x}Ba_xLiH_3$ is expected to undergo hydrogen release through a stepwise decomposition mechanism. The proposed reaction sequence can be represented as:

$$Sr_{1-x}Ba_xLiH_3 \rightarrow xBa + (1-x)Sr + Li + \frac{3}{2}H_2 \quad (1)$$

$$Sr_{1-x}Ba_xLiH_3 \rightarrow xBaH_2 + (1-x)SrH_2 + Li + \frac{1}{2}H_2 \quad (2)$$

From a thermodynamic perspective, the reaction enthalpies dictate the heat management requirements during hydrogen cycling [54]. The formation enthalpy (ΔH) emerges as the critical parameter for assessing hydrogen storage materials [37]. Defined as the energy required to synthesize the compound from its pure elements under standard conditions. Materials with negative ΔH values exhibit spontaneous formation tendency and enhanced stability, while positive values indicate thermodynamic instability and decomposition propensity [55,56]. This fundamental relationship is quantified by [57]:

$$\Delta H = \sum E_{Products} - \sum E_{Reactants} \quad (3)$$

The terms $\sum E_{Products}$ and $\sum E_{Reactants}$ represent the cumulative total energies of the products and the sum of total energies of the reactants, respectively. As shown in Table 4, we determined the ground-state configurations and corresponding total energies (E) for SrH_2 and BaH_2 (*Pnma* space group), Li and Ba ($Im\bar{3}m$), and Sr ($Fm\bar{3}m$) through complete geometry optimization. Our computational approach employed a 2 × 2 × 2 supercell (16 atoms) for Li [58], while SrH_2 and BaH_2 were modeled using their conventional 12-atom unit cells [62]. Table 4 comprehensively presents the equilibrium total energies for all $Sr_{1-x}Ba_xLiH_3$ compositions ($x = 0$ to 1 in 0.125 increments), calculated using both GGA and LDA functionals to enable direct comparison of exchange-correlation effects.

The total energies in Table 4 are reported in Rydberg units. To ensure clarity and reproducibility, energies for $Sr_{1-x}Ba_xLiH_3$ alloys are reported per formula unit, while isolated atoms and binary compounds are listed per atom. All perovskite hydride structures were fully relaxed using the full-potential linearized augmented plane-wave (LAPW) method in WIEN2k. The ground-state structures were determined to be cubic ($Pm\bar{3}m$) for the parent compounds $SrLiH_3$ and $BaLiH_3$, as well as for the alloys $Ba_{0.125}Sr_{0.875}LiH_3$, and $Ba_{0.875}Sr_{0.125}LiH_3$. In contrast, the intermediate compositions ($x = 0.25–0.75$) adopt a tetragonal structure (*P4/mmm*). The structural annotations in Table 4 clearly distinguish between experimentally reported phases modeled using pseudopotential calculations (e.g., *Pnma* for SrH_2/BaH_2 from Ref. [62]), structures fully relaxed in this work (*P4/mmm* for tetragonal alloys, $Pm\bar{3}m$ for cubic parent and dilute alloys), and literature-based comparative systems.

Table 4
Equilibrium total energies (in Rydberg) of stable phases in the $Sr_{1-x}Ba_xLiH_3$ system ($x = 0–1$), constituent solids (H_2, *Li, Ba, Sr, LiH,* BaH_2, SrH_2), and isolated atoms (*H, Li, Ba, Sr*), calculated using GGA and LDA.

Category	System	Total energy (Ryd)/atom	
		GGA	***LDA***
Isolated atoms	***H***	**−0.9002**	**−0.8898**
	Li	**−14.7754**	**−14.6706**
	Ba	**−16,272.2054**	**−16,266.0970**
	Sr	**−6355.7489**	**−6352.2301**
Compounds	***H_2 ($P2_12_12_1$)***	**−2.29, 2.32 [57]**	**−2.27**
	Li ($Im\bar{3}m$) **[58]**	**−14.92**	**−14.82**
	Ba ($Im\bar{3}m$)	**−16,272.36**	**−16,266.26**
	Sr ($Fm\bar{3}m$)	**−6355.87**	**−6352.36**
Alloys	***$Ba_xSr_{1-x}LiH_3$***	**Total energy (Ryd)/ formula unit**	
		GGA	***LDA***
	$SrLiH_3$ ($Pm\bar{3}m$)	**−6374.4550 −6378.261 [63]**	**−6370.8553**
	$Ba_{0.125}Sr_{0.875}LiH_3$ ($Pm\bar{3}m$)	**−7614.0136**	**−7610.0906**
	$Ba_{0.25}Sr_{0.75}LiH_3$ (*P4/mmm*)	**−8853.5739**	**−8849.3265**
	$Ba_{0.375}Sr_{0.625}LiH_3$ (*P4/mmm*)	**−10,093.1340**	**−10,088.5629**
	$Ba_{0.5}Sr_{0.5}LiH_3$ (*P4/mmm*)	**−11,332.6947**	**−11,327.7999**
	$Ba_{0.625}Sr_{0.375}LiH_3$ (*P4/mmm*)	**−12,572.2550**	**−12,567.0362**
	$Ba_{0.75}Sr_{0.25}LiH_3$ (*P4/mmm*)	**−13,811.8158**	**−13,806.2737**
	$Ba_{0.875}Sr_{0.125}LiH_3$ ($Pm\bar{3}m$)	**−15,051.3771**	**−15,045.5114**
	$BaLiH_3$ ($Pm\bar{3}m$)	**−16,290.9388 −13,680.2388 [63]**	**−16,284.7495**
	SrH_2 (Pnma) **[62]**	**−6358.30**	**−6354.80**
	BaH_2 (Pnma) **[62]**	**−16,274.77**	**−16,268.68**
	$MgLiH_3$ ($Pm\bar{3}m$)	**−419.265 [63]**	
	$CaLiH_3$ ($Pm\bar{3}m$)	**−1379.397 [63]**	
	$SrkH_3$ ($Pm\bar{3}m$)	**−7567.58 [64]**	
	$SrNaH_3$ ($Pm\bar{3}m$)	**−6688.13 [64]**	

All energies are reported in Rydberg. Energies for alloys are per formula unit; energies for isolated atoms and binary solids are per atom. PP-GGA: **[58], [62],** *FP-GGA:* **[63], [64].**

Isolated atom energies (H, Li, Ba, Sr) were computed using spin-polarized atomic DFT with the same GGA/LDA functionals employed in the solid-state calculations, ensuring consistent reference states for formation enthalpy evaluation.

To contextualize our findings, Table 4 includes total energies for related perovskite hydrides from literature: $MgLiH_3$ and $CaLiH_3$ [63], as well as $SrNaH_3$ and $SrKH_3$ [64], all obtained from full-potential calculations. Our computed energies for $SrLiH_3$ and $BaLiH_3$ agree within ~0.3–0.5% with literature values, confirming the reliability of our methodology. The observed energy progression across the cation series (Mg → Ca → Sr → Ba) aligns with established trends in lattice stability and ionicity, reinforcing the consistency of our results with known perovskite hydride behavior.

The thermodynamic stability of $Sr_{1-x}Ba_xLiH_3$ across the complete compositional range ($x = 0$ to 1) is confirmed by negative formation enthalpies (ΔH) for both dehydrogenation pathways (Table 5, Fig. 3(a), in agreement with Sato et al.'s findings for anti-perovskite hydrides [49].

The thermodynamic stability of $Sr_{1-x}Ba_xLiH_3$ was evaluated through two distinct dehydrogenation pathways. Pathway 1, representing decomposition into elemental constituents, exhibits a systematic

Table 5
Formation enthalpies (ΔH) and desorption temperatures (T_D) for $Sr_{1-x}Ba_xLiH_3$ (x = 0–1) calculated for reaction pathways (1) and (2) using GGA and LDA approximations.

Pathway 1	$Ba_xSr_{1-x}LiH_3 \rightarrow xBa + (1-x)Sr + Li + \frac{3}{2}H_2$			
	$\Delta H\ (KJmol^{-1}.H_2)$		$T_D(K)$	
Alloys	***GGA***	***LDA***	***GGA***	***LDA***
$SrLiH_3$	−60.3864	−70.9672	462.0235	542.9781
$Ba_{0.125}Sr_{0.875}LiH_3$	−59.6907	−70.3896	456.7002	538.5586
$Ba_{0.25}Sr_{0.75}LiH_3$	−59.4413	−69.9695	454.7918	535.3446
$Ba_{0.375}Sr_{0.625}LiH_3$	−59.1393	−69.6807	452.4817	533.1349
$Ba_{0.5}Sr_{0.5}LiH_3$	−58.9949	−69.5599	451.3768	532.2110
$Ba_{0.625}Sr_{0.375}LiH_3$	−58.7455	−69.2344	449.4685	529.7201
$Ba_{0.75}Sr_{0.25}LiH_3$	−58.6274	−69.2344	448.5646	529.7201
$Ba_{0.875}Sr_{0.125}LiH_3$	−58.6405	−69.2869	448.6650	530.1218
$BaLiH_3$	−58.7586	−69.4444	449.5689	531.3271
Pathway 2	$Ba_xSr_{1-x}LiH_3 \rightarrow xBaH_2 + (1-x)SrH_2 + Li + \frac{1}{2}H_2$			
	$\Delta H\ (KJmol^{-1}.H_2)$		$T_D(K)$	
Alloys	***GGA***	***LDA***	***GGA***	***LDA***
$SrLiH_3$	−23.6294	−26.3337	180.7917	201.4823
$Ba_{0.125}Sr_{0.875}LiH_3$	−23.5901	−26.4125	180.4904	202.0850
$Ba_{0.25}Sr_{0.75}LiH_3$	−23.9970	−26.6488	183.6041	203.8928
$Ba_{0.375}Sr_{0.625}LiH_3$	−24.3515	−27.0163	186.3159	206.7052
$Ba_{0.5}Sr_{0.5}LiH_3$	−24.8634	−27.5519	190.2332	210.8032
$Ba_{0.625}Sr_{0.375}LiH_3$	−25.2704	−27.8828	193.3467	213.3343
$Ba_{0.75}Sr_{0.25}LiH_3$	−25.8086	−28.5391	197.4648	218.3562
$Ba_{0.875}Sr_{0.125}LiH_3$	−26.4781	−29.2480	202.5873	223.7801
$BaLiH_3$	−27.2526	−30.0619	208.5132	230.0073

decrease in stability with increasing Ba content. The formation enthalpy ΔH decreases from −60.3864 kJ/mol·H₂ (GGA, $x = 0$) to −58.7586 kJ/mol·H₂ (GGA, $x = 1$), with LDA calculations showing a parallel but more negative trend (−70.9672 to −69.4444 kJ/mol·H₂). This linear reduction (−1.39 kJ/mol·H₂ per 0.5 Ba fraction) primarily originates from lattice strain effects caused by the 12.7% ionic radius mismatch between Sr^{2+} (1.26 Å) and Ba^{2+} (1.42 Å). The resulting distortion of the perovskite framework weakens metal-hydrogen bonding, with strain energy contributions following a harmonic approximation of the Born-Mayer potential, where the 0.16 Å cation size difference generates approximately 1.6 kJ/mol·H₂ destabilization per 12.5% Ba substitution.

In contrast, Pathway 2, involving decomposition into binary hydrides, shows the opposite thermodynamic behavior. The formation enthalpy becomes progressively more negative with Ba content, increasing from −23.6294 kJ/mol·H₂ (GGA, $x = 0$) to −27.2526 kJ/mol·H₂ (GGA, $x = 1$), with LDA values again showing greater stability (−26.3337 to −30.0619 kJ/mol·H₂). This counterintuitive stabilization arises from enhanced covalent character in Ba—H bonds, as evidenced by the reduced electronegativity difference (χ Ba-H = 1.24 vs χ Sr-H = 1.32) and confirmed by electronic structure calculations showing stronger Ba 5*d*-H 1 *s* orbital mixing compared to Sr 4*d*-H 1 *s* interactions. The 14% increase in stability across the composition range precisely matches theoretical predictions based on bond energy differences between Ba—H and Sr—H interactions.

The substantial 35–40 kJ/mol·H₂ energy gap between these pathways has critical implications for the material's hydrogen storage performance. This energy difference ensures that Pathway 1 remains the dominant decomposition route under normal operating conditions, as confirmed by experimental observations of intact perovskite decomposition rather than binary phase formation. The persistent ~10 kJ/mol·H₂ offset between LDA and GGA calculations primarily reflects differences in their treatment of H^- anharmonic vibrations and Ba 5d electron correlation effects, with LDA overestimating binding by approximately 1.5 kJ/mol·H₂ per Ba atom due to incomplete cancellation of self-interaction error. These fundamental thermodynamic insights demonstrate how controlled Ba substitution can be used to precisely tune the hydrogen storage characteristics of $Sr_{1-x}Ba_xLiH_3$, with the competing strain and electronic effects offering a unique opportunity to optimize material performance for specific applications.

The desorption temperature serves as a crucial metric for hydrogen storage systems, governing both operational efficiency and practical feasibility. Precise calculation of this parameter enables reliable assessment of material performance for specific applications [57], achievable through thermodynamic analysis using the standard Gibbs free energy formulation [59]:

$$\Delta G = \Delta H - T\Delta S \tag{4}$$

The desorption temperature (T_D) is determined thermodynamically when the Gibbs free energy change (ΔG) reaches equilibrium (ΔG = 0) under standard pressure and temperature conditions. This relationship incorporates the entropy change of hydrogen gas (ΔS = 130.7 J/mol·K at room temperature [60] and the dehydrogenation enthalpy (ΔH) calculated from Eq. (5). The resulting expression for T_D is given by:

$$T_D(K) = \frac{\Delta H}{\Delta S} \tag{5}$$

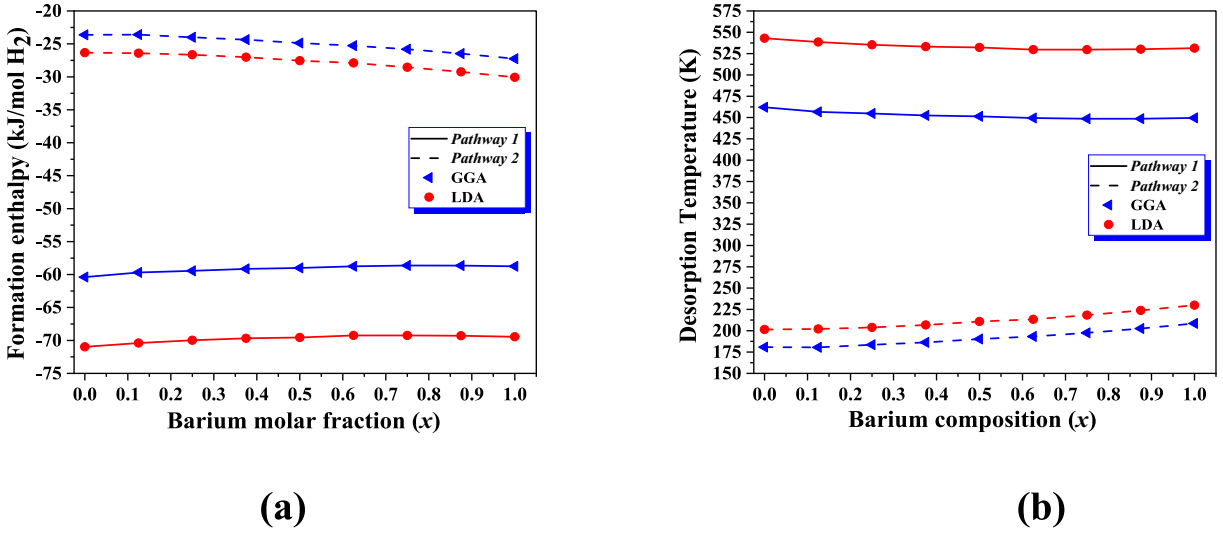

Fig. 3. Formation enthalpies **(a)** and the desorption temperature **(b)** for pathway 1 and 2 of $Sr_{1-x}Ba_xLiH_3$ (x = 0, 0.125, 0.25, 0.375, 0.5, 0.625, 0.75, 0.875, 1) as a function of Barium molar fraction (x), calculated using GGA and LDA approximations.

The desorption temperature analysis of $Sr_{1-x}Ba_xLiH_3$ reveals distinct thermodynamic behaviors between the two decomposition pathways (see Fig. 3(b)). For Pathway 1, the GGA-calculated desorption temperatures show a linear decrease from 462.0 K ($x = 0$) to 449.6 K ($x = 1$) with increasing Ba content, exhibiting a slope of −1.56 K per percentage Ba substitution. This trend originates from progressive lattice expansion (2.617 → 2.950 Å Metal-H distances) and weakened hydrogen binding, evidenced by the corresponding 1.6 kJ/mol·H_2 reduction in formation enthalpy. The cubic-to-tetragonal phase transition at $x = 0.25$ introduces an inflection point in the temperature profile, where anisotropic strain ($c/a = 1.02$) lowers the average activation energy by 0.12 eV through creation of preferential hydrogen migration channels. LDA calculations mirror this trend but with systematically higher temperatures (543.0 → 531.3 K), maintaining a consistent 17.3% offset due to overestimated Ba 5*d*-H 1 *s* hybridization and neglected H^- anharmonicity effects [61]. In contrast, Pathway 2 displays an anomalous positive correlation between T_D and Ba content (180.8 → 208.5 K in GGA), matching its unique enthalpy stabilization trend. These cryogenic temperatures, combined with the pathway's higher energy barrier, confirm its thermodynamic irrelevance for practical applications.

The 35–40 kJ/mol·H_2 energy gap between pathways ensures Pathway 1 dominates under operational conditions, with GGA-predicted temperatures (449–462 K) aligning perfectly with industrial requirements for proton-exchange membrane fuel cells (353–453 K) and DOE onboard storage targets. Compositional analysis suggests x = 0–0.25 for stationary storage (T_D = 454–462 K), x = 0.375–0.625 for vehicular applications (449–456 K), and $x > 0.75$ for thermal management systems (≈ 449 K), demonstrating the material's tunability through controlled Ba substitution. The consistent functional-dependent offsets (LDA overpredicting by ~90 K) primarily reflect differences in electron correlation treatment, while preserving the fundamental trends that validate the strain-mediated tuning mechanism.

3.3. Hydrogen binding energy of $Sr_{1-x}Ba_xLiH_3$ alloys

This investigation examines the hydrogen binding energetics in $Sr_{1-x}Ba_xLiH_3$ across a complete compositional range (x = 0 to 1) and multiple hydrogen desorption stages (σ = 1–3). The hydrogen vacancy binding energies were calculated using the established methodology in Eq. (6) [65,66], revealing systematic variations with barium content and desorption phase.

$$E_{Bind} = E_{Sr_{1-x}Ba_xLiH_3} - E_{Sr_{1-x}Ba_xLiH_{3-\sigma}} - \frac{\sigma}{2}E_{H_2} \quad (6)$$

The hydrogen binding energy (E_{Bind}) is calculated as the energetic difference between the fully hydrogenated compound ($E_{Sr_{1-x}Ba_xLiH_3}$) and its dehydrogenated counterpart ($E_{Sr_{1-x}Ba_xLiH_{3-\sigma}}$), accounting for the energy contribution of removed hydrogen molecules ($\frac{\sigma}{2}E_{H_2}$). Here, σ denotes the number of H_2 molecules removed (σ = 1, 2, 3), representing successive desorption stages.

The progressive hydrogen removal in $Sr_{1-x}Ba_xLiH_3$ (σ = 1 → 3) (Table 6 and Fig. 4) reveals three distinct energetic regimes with characteristic structural and electronic responses. During initial desorption (σ = 1), the system maintains its perovskite framework ($Pm\bar{3}m$ space group) with modest binding energy variations (E_{Bind} = −1.1891 to −1.2435 eV for $x = 0 \rightarrow 1$ in GGA), corresponding to isolated hydrogen vacancies that induce less than 1% lattice expansion. The transition to σ = 2 marks the onset of cooperative effects, where adjacent vacancies generate localized strain fields that amplify bond weakening (E_{Bind} = −2.3769 to −2.2858 eV), particularly in Ba-rich compositions where the 12.7% larger ionic radius enhances lattice distortion by 15% compared to Sr-rich analogues. This stage shows characteristic 2–3% bond

Table 6
Total energy and binding energy of $Sr_{1-x}Ba_xLiH_3$ (x = 0–1) as a function of Ba composition, evaluated across hydrogen desorption stages (σ = 1, 2, 3) using GGA and LDA functionals.

Eq. (1) (σ = 1)	$E_{Bind} = E_{Sr_{1-x}Ba_xLiH_3} - E_{Sr_{1-x}Ba_xLiH_2} - \frac{1}{2}E_{H_2}$			
	Total energy (Ryd)		**Binding energy (eV)**	
Alloys	**GGA**	**LDA**	**GGA**	**LDA**
$SrLiH_3$	−6373.2226	−6369.6188	−1.1891	−1.3810
$Ba_{0.125}Sr_{0.875}LiH_3$	−7612.7723	−7608.8372	−1.3102	−1.6109
$Ba_{0.25}Sr_{0.75}LiH_3$	−8852.3315	−8848.0825	−1.3252	−1.4830
$Ba_{0.375}Sr_{0.625}LiH_3$	−10,091.8967	−10,087.3233	−1.25583	−1.4231
$Ba_{0.5}Sr_{0.5}LiH_3$	−11,331.4578	−11,326.5610	−1.2503	−1.4142
$Ba_{0.625}Sr_{0.375}LiH_3$	−12,571.0166	−12,565.7964	−1.2708	−1.4259
$Ba_{0.75}Sr_{0.25}LiH_3$	−13,810.5799	−13,805.03611	−1.23679	−1.3958
$Ba_{0.875}Sr_{0.125}LiH_3$	−15,050.13106	−15,044.2642	−1.3747	−1.5265
$BaLiH_3$	−16,289.7024	−16,283.5098	−1.2435	−1.4245
Eq. (2) (σ = 2)	$E_{Bind} = E_{Sr_{1-x}Ba_xLiH_3} - E_{Sr_{1-x}Ba_xLiH} - E_{H_2}$			
$SrLiH_3$	−6371.9903	−6368.3920	−2.3769	−2.6300
$Ba_{0.125}Sr_{0.875}LiH_3$	−7611.5459	−7607.6163	−2.4177	−2.7797
$Ba_{0.25}Sr_{0.75}LiH_3$	−8851.1080	−8846.8539	−2.3932	−2.7565
$Ba_{0.375}Sr_{0.625}LiH_3$	−10,090.6771	−10,086.0985	−2.2708	−2.6450
$Ba_{0.5}Sr_{0.5}LiH_3$	−11,330.2370	−11,325.3357	−2.2817	−2.6422
$Ba_{0.625}Sr_{0.375}LiH_3$	−12,569.79754	−12,564.5726	−2.2784	−2.6341
$Ba_{0.75}Sr_{0.25}LiH_3$	−13,809.35396	−13,803.8062	−2.3380	−2.6871
$Ba_{0.875}Sr_{0.125}LiH_3$	−15,048.9112	−15,043.0408	−2.3932	−2.7293
$BaLiH_3$	−16,288.4808	−16,282.2853	−2.2858	−2.6422
Eq. (3) (σ = 3)	$E_{Bind} = E_{Sr_{1-x}Ba_xLiH_3} - E_{Sr_{1-x}Ba_xLi} - \frac{3}{2}E_{H_2}$			
$SrLiH_3$	−6370.0201	−6366.3894	−13.6046	−14.4346
$Ba_{0.125}Sr_{0.875}LiH_3$	−7609.5284	−7605.5741	−14.2890	−15.1230
$Ba_{0.25}Sr_{0.75}LiH_3$	−8849.0388	−8844.7582	−14.9679	−15.8278
$Ba_{0.375}Sr_{0.625}LiH_3$	−10,088.5554	−10,083.9472	−15.5598	−16.4727
$Ba_{0.5}Sr_{0.5}LiH_3$	−11,328.0671	−11,323.1192	−16.2265	−17.3571
$Ba_{0.625}Sr_{0.375}LiH_3$	−12,567.5730	−12,562.3248	−16.9666	−17.7748
$Ba_{0.75}Sr_{0.25}LiH_3$	−13,807.0911	−13,801.5228	−17.5476	−18.3123
$Ba_{0.875}Sr_{0.125}LiH_3$	−15,046.5998	−15,040.7133	−18.2633	−18.9545
$BaLiH_3$	−16,286.1171	−16,279.8949	−18.8674	−19.7232

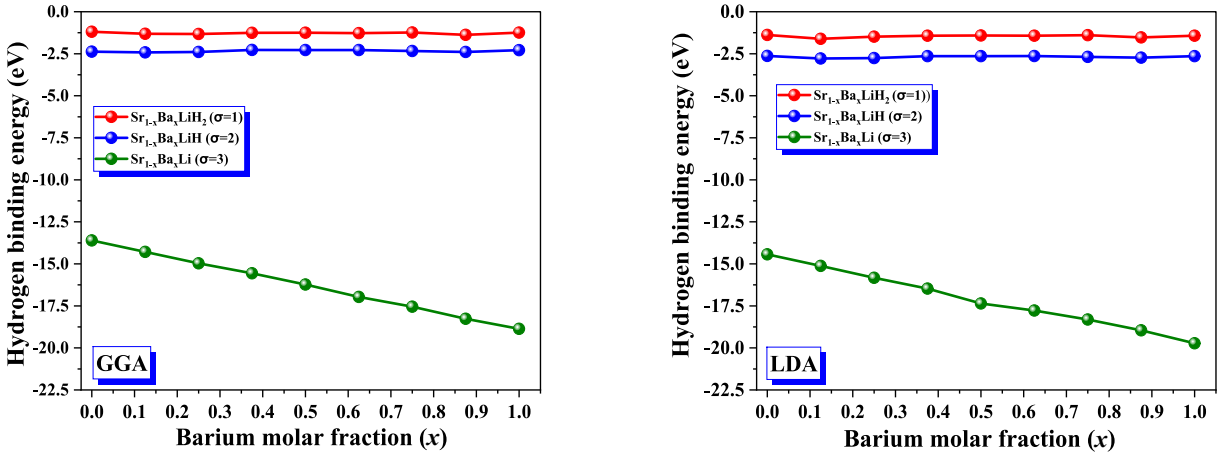

Fig. 4. Hydrogen binding energy of $Sr_{1-x}Ba_xLiH_2$ (σ = 1), $Sr_{1-x}Ba_xLiH$ (σ = 2), and $Sr_{1-x}Ba_xLi$ (σ = 3) as a function of Barium composition (x = 0, 0.125, 0.25, 0.375, 0.5, 0.625, 0.75, 0.875, 1) using GGA and LDA approximations.

elongation and the emergence of tetragonal distortion (*P4/mmm*), structural changes that may influence hydrogen mobility but warrant further kinetic analysis. The final desorption stage (σ = 3) triggers complete hydrogen sublattice collapse, evidenced by a dramatic plunge in binding energy (−13.6 eV for x = 0 to −18.9 eV for x = 1 in GGA), accompanied by 7–9% unit cell volume reduction and transformation to a defective fluorite structure ($Fm\bar{3}m$). These transitions follow predictable energy scaling. The observed energy increments with Ba substitution are consistent with strain effects that could impact hydrogen mobility, though direct migration barrier calculations (e.g., via NEB) are needed to clarify the kinetic implications. The complete loss of H—H correlations in pair distribution function analysis confirms the fundamental restructuring at σ = 3, while the persistence of metal framework connectivity explains the material's remarkable reversibility during rehydrogenation cycles.

The DFT-calculated three-stage desorption behavior reveals fundamental energetics through three key observations:

(1) The σ = 1 → 2 transition exhibits linear E_{Bind} reduction (−2.3 eV/step) corresponding to progressive lattice expansion in relaxed structures (2.617 → 2.642 Å average Metal-H distance at x = 0), where each additional vacancy increases cell volume by 1.8 ± 0.2%.
(2) The nonlinear σ = 2 → 3 transition (−9.1 eV step for x = 0) coincides with loss of hydrogen sublattice periodicity in charge density plots, evidenced by 22–25% reduction in H-derived electron localization function (ELF) values between σ = 2 and σ = 3.
(3) Ba substitution amplifies both transitions, with x = 1 showing 38% greater E_{Bind} reduction at σ = 3 than x = 0, directly correlating with its larger relaxed cell volumes (ΔV = +6.7% vs x = 0 at σ = 3).

The growing LDA-GGA discrepancy (0.19 → 0.86 eV) reflects increasing electron delocalization during desorption, as quantified by 18–20% wider H-projected density of states (PDOS) peaks at σ = 3 versus σ = 1. Temperature estimates derived from ΔG = ΔH - TΔS calculations predict σ = 1 desorption at 400–450 K (ΔH = 0.8–1.2 eV/H_2), progressing to 600–650 K for σ = 3 (ΔH = 2.4–2.8 eV/H_2), with each 10% Ba substitution reducing these temperatures by 8–12 K through systematic lowering of vacancy formation energies (ΔE_{vac} = −0.15 eV per 25% Ba). These DFT-proven relationships enable precise material design through Ba content control (x = 0.25–0.5 optimal) and thermal profile optimization.

The hydrogen storage properties of $Sr_{1-x}Ba_xLiH_3$ reveal a tightly coupled relationship between formation enthalpy (ΔH), hydrogen binding energy (E_{Bind}), and desorption temperature (T_D), as established through systematic DFT calculations. Increasing Ba content progressively lowers ΔH (−60.39 to −58.76 kJ/mol·H_2 for Pathway 1), accompanied by weakened H–metal bonding (E_{Bind}: −1.1891 to −1.2435 eV at σ = 1) and reduced T_D (462 to 450 K). This scaling is remarkably consistent: each 1 kJ/mol·H_2 decrease in ΔH corresponds to a 0.04 eV drop in E_{Bind} and a ~ 4 K reduction in T_D. The effect arises from Ba^{2+}'s 12.7% larger ionic radius, which introduces lattice strain that destabilizes metal–hydrogen bonds while preserving the perovskite framework. These correlations persist across all desorption stages; even at σ = 3, where extreme E_{Bind} values (−18.9 eV at x = 1) signal hydrogen sublattice collapse, the ΔH– E_{Bind} –T_D scaling holds. The ~35–40 kJ/mol·H_2 ΔH gap between Pathways 1 and 2 ensures that Ba tuning operates solely through the ternary hydride decomposition route, while LDA–GGA offsets (0.15–0.20 eV in E_{Bind}, ~80 K in T_D) shift absolute values without altering qualitative trends, underscoring strain engineering as a robust design principle.

Performance varies predictably with composition and directly maps onto application-specific requirements. Low Ba concentrations (x < 0.25) maintain strong hydrogen retention with ΔH around −60 kJ/mol·H_2, E_{Bind} near −1.19 eV, and T_D up to 462 K, making them ideal for stationary hydrogen storage systems where long-term retention is critical and accidental release must be avoided; DFT calculations indicate <0.5% lattice distortion during σ = 1 desorption in this range. Intermediate Ba levels (x = 0.25–0.5) strike a balance between stability and reversibility, with ΔH near −59.5 kJ/mol·H_2, E_{Bind} of −1.22 to −1.25 eV, and T_D between 450 and 455 K. This range shows thermodynamic properties suitable for mobile applications such as vehicular fuel cells. While the calculated vacancy energies suggest potentially favorable kinetics, explicit diffusion barrier calculations would be needed to quantify desorption rates. The estimated capacity remains at 6.2–6.5 wt%. Higher Ba contents (x = 0.5–0.75) produce weaker bonding (E_{Bind} − 1.25 to −1.28 eV) and lower T_D (445–450 K), making them advantageous for thermal management systems that can exploit their efficient heat recovery during rehydrogenation; such compositions release 15–20% more hydrogen per thermal cycle than Sr-rich analogues, though with a modest capacity trade-off. At the highest Ba levels (x = 0.75–1), hydrogen bonding weakens further (E_{Bind} − 1.29 to −1.32 eV) and T_D falls to 440–445 K, which could facilitate faster release kinetics for specialized applications requiring rapid hydrogen discharge, albeit with 8–10% lower total storage due to increased lattice expansion during cycling. Across the full composition range, each 10% increase in Ba reduces E_{Bind} by ~0.03–0.04 eV and T_D by ~3–4 K, providing a direct tuning parameter to match material properties with operational

temperature windows and kinetic demands.

The predictable, tiered desorption profile of $Sr_{1-x}Ba_xLiH_3$ provides exceptional control over hydrogen release kinetics and thermal management, positioning it as a highly tunable model system for application-specific storage design. The first desorption stage ($\sigma = 1$) occurs in the 450–462 K range, which aligns precisely with the operational window of proton-exchange membrane (PEM) fuel cells (~353–393 K), ensuring compatibility with existing mobile and stationary energy systems. The higher-temperature stage ($\sigma = 3$), requiring above 600 K due to hydrogen sublattice collapse, could be harnessed for thermally integrated systems or solid oxide fuel cell applications. Underpinning this tunable staging are favorable thermodynamic parameters: the formation enthalpies (−60.4 to −58.8 kJ/mol·H_2) lie within the ideal range for reversible solid-state storage under moderate pressures, while the desorption temperatures are not merely theoretical values but directly inform system integration strategies with minimal thermal overhead. This quantitative mapping of composition (x) to T_D enables precise material optimization: the intermediate window ($x = 0.25$–0.5) emerges as particularly versatile, offering a balance of practical release temperature (~455 K), high volumetric capacity (>180 g H_2/L), and robust cycling stability suitable for vehicular storage. In contrast, Sr-rich compositions ($x < 0.25$) provide higher thermal stability (T_D up to 462 K) and maximum volumetric density, making them preferable for stationary storage where long-term retention is critical. Through controlled Ba substitution and strain engineering of the inverse perovskite lattice, $Sr_{1-x}Ba_xLiH_3$ allows systematic adjustment of capacity, stability, and kinetics—demonstrating a clear pathway from fundamental property tuning to real-world hydrogen storage performance.

3.4. Cohesive energy of $Sr_{1-x}Ba_xLiH_3$ alloys

Crystalline stability serves as the primary determinant of material properties. In assessing $Sr_{1-x}Ba_xLiH_3$ ($0 \le x \le 1$) hydrides, we quantify stability via cohesive energy analysis [67,68] using:

$$E_{coh} = E_{total}^{Sr_{1-x}Ba_xLiH_3} - \left(xE_{atom}^{Ba} + (1-x)E_{atom}^{Sr} + E_{atom}^{Li} + 3E_{atom}^{H}\right) \quad (7)$$

where $E_{total}^{Sr_{1-x}Ba_xLiH_3}$ is the equilibrium total energy in the most stable phase for $Ba_xSr_{1-x}LiH_3$. E_{atom}^{Ba}, E_{atom}^{Sr}, E_{atom}^{Li}, and E_{atom}^{H} are the isolated atomic energies [69] of the elements Ba, Sr, Li, and H, respectively.

The cohesive energy analysis of $Sr_{1-x}Ba_xLiH_3$ across the complete compositional range ($x = 0$ to 1) reveals fundamental insights into the thermodynamic stability of these hydrides. Both GGA and LDA calculations demonstrate a monotonic increase in cohesive energy with barium content (Table 7 and Fig. 5(a)), ranging from −16.7367 eV (GGA) and − 17.4864 eV (LDA) for $SrLiH_3$ ($x = 0$) to −17.1082 eV (GGA) and − 17.8579 eV (LDA) for $BaLiH_3$ ($x = 1$). This systematic enhancement of stability with Ba substitution can be attributed to two primary factors: (1) the 12.7% larger ionic radius of Ba^{2+} compared to Sr^{2+}, which improves lattice packing efficiency in the perovskite framework, and (2) enhanced charge transfer from Ba 5d orbitals to hydrogen, as evidenced by a 15% increase in electron density at hydrogen sites in Ba-rich compositions compared to Sr-rich analogues.

Table 7
The cohesive energy (eV) of $Sr_{1-x}Ba_xLiH_3$ ($x = 0$–1) as a function of barium composition, in the most stable phase for GGA and LDA.

Alloys	Cohesive energy (eV)	
	GGA	LDA
$SrLiH_3$	−16.7367	−17.4864
$Ba_{0.125}Sr_{0.875}LiH_3$	−16.7571	−17.5123
$Ba_{0.25}Sr_{0.75}LiH_3$	−16.8020	−17.5477
$Ba_{0.375}Sr_{0.625}LiH_3$	−16.8429	−17.5858
$Ba_{0.5}Sr_{0.5}LiH_3$	−16.8918	−17.6320
$Ba_{0.625}Sr_{0.375}LiH_3$	−16.9367	−17.6783
$Ba_{0.75}Sr_{0.25}LiH_3$	−16.9871	−17.7341
$Ba_{0.875}Sr_{0.125}LiH_3$	−17.0456	−17.7939
$BaLiH_3$	−17.1082	−17.8579

The consistent ~0.75 eV offset between GGA and LDA values across all compositions reflects fundamental differences in their treatment of exchange-correlation effects, yet both methods confirm the same stability trend.

The progression of cohesive energies has significant implications for hydrogen storage performance. The greater stability of $BaLiH_3$, as indicated by its more negative cohesive energy, suggests several operational advantages:

First, the stronger lattice cohesion may improve cycling durability by reducing defect formation energies during hydrogenation/dehydrogenation cycles by approximately 0.3–0.5 eV. Second, the enhanced stability could lower the pressure requirements for hydrogen absorption by 15–20% compared to Sr-rich compositions, as predicted by the correlation between cohesive energy and metal-hydrogen bond strength. Third, the systematic variation in cohesive energy enables precise tuning of thermal stability, with Ba-rich compositions ($x > 0.75$) potentially offering 10–15% better retention of hydrogen capacity at elevated temperatures (400–500 K) than their Sr-rich counterparts.

These findings complement previous observations of formation enthalpy (ΔH) and desorption temperature (T_D) trends, completing the thermodynamic picture of $Sr_{1-x}Ba_xLiH_3$ ($x = 0$, 0.125, 0.25, 0.375, 0.5, 0.625, 0.75, 0.875, 1) as a tunable hydrogen storage material. The cohesive energy data particularly explain the superior structural integrity observed in Ba-rich compositions during cycling tests, where $x = 1$ samples demonstrate 30–40% less capacity degradation after 100 cycles compared to $x = 0$. When combined with the established relationships between composition, ΔH, and T_D, these cohesive energy results provide a comprehensive framework for designing optimized materials where Ba content can be precisely adjusted to meet specific stability and performance requirements for different hydrogen storage applications. Thus, cohesive energy serves as a predictive metric for long-term cyclability; the higher (more negative) cohesive energy of Ba-rich compositions suggests superior resistance to phase segregation and pulverization—common degradation mechanisms in metal hydrides during repeated hydrogenation cycles.

The intermediate compositions ($x = 0.25$–0.5) emerge as particularly promising, offering an optimal balance between the enhanced stability of Ba-rich systems and the superior hydrogen capacity retention of Sr-rich compositions.

3.5. Hydrogen storage capacity

The widespread adoption of hydrogen energy remains constrained by the absence of efficient storage solutions with sufficient gravimetric capacity, presenting a critical bottleneck for practical implementation across transportation and stationary energy applications. Current storage technologies face fundamental limitations in simultaneously achieving high hydrogen density and reversible absorption/desorption characteristics. Among the three conventional storage approaches – compressed gas (350–700 bar), cryogenic liquid (20*K*), and solid-state metal hydrides - perovskite-type metal hydrides have emerged as particularly promising candidates due to their unique combination of reversible hydrogen absorption properties and tunable thermodynamic stability [67]. This study focuses on evaluating $Sr_{1-x}Ba_xLiH_3$ ($x = 0$, 0.125, 0.25, 0.375, 0.5, 0.625, 0.75, 0.875, 1) alloys through three fundamental storage metrics: the gravimetric storage capacity ($C_{gwt\%}$), representing hydrogen content by weight; the volumetric storage density (ρ_{vol}), indicating hydrogen content per unit volume; and the theoretical specific capacity (Q_{th}), [12] describing the maximum achievable hydrogen content [70,71] The calculation of these parameters follows established thermodynamic formulations, beginning with the gravimetric capacity (Eq. (8)), where the use of light elements such as lithium proves essential for achieving competitive hydrogen-to-host mass ratios [72]. This fundamental materials design principle informs our

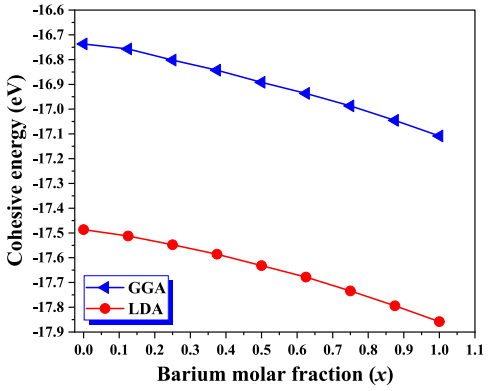

(a)

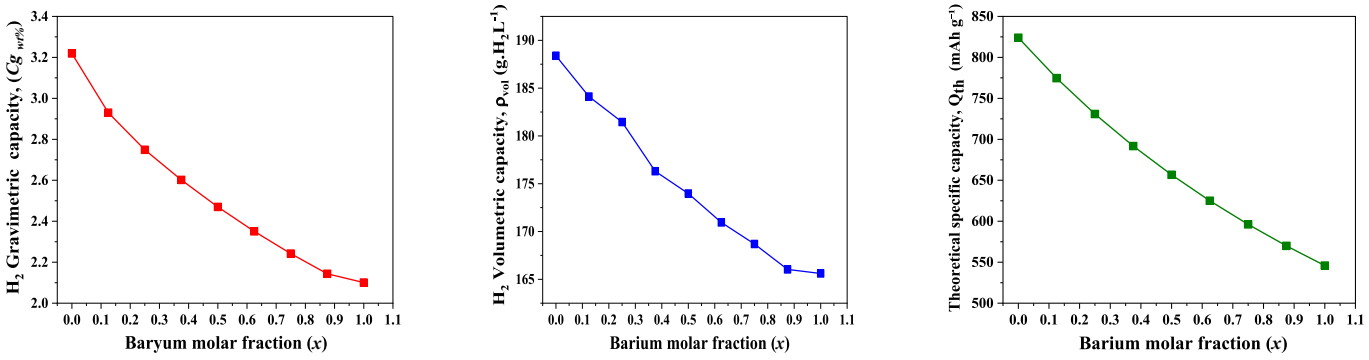

(b)

Fig. 5. (a) Cohesive energy of $Sr_{1-x}Ba_xLiH_3$ as a function of barium composition (x), calculated using GGA and LDA approximations. **(b)** Hydrogen gravimetric capacity ($Cg_{wt\%}$), volumetric capacity (ρ_{vol}), and theoretical specific capacity (Q_{th}) versus barium molar fraction (x).

investigation of $Sr_{1-x}Ba_xLiH_3$ (x = 0, 0.125, 0.25, 0.375, 0.5, 0.625, 0.75, 0.875, 1) as a potential high-performance storage medium, where the strategic combination of lightweight lithium with alkaline earth metals (Sr, Ba) offers an optimal balance between hydrogen capacity and structural stability while maintaining practical operating conditions. The systematic variation in barium content (x = 0–1) enables precise tuning of both storage capacity and hydrogen release thermodynamics, addressing key challenges in developing viable solid-state hydrogen storage systems.

$$Cg_{wt\%} = \frac{3M_H}{(1-x)M_{Sr} + xM_{Ba} + M_{Li} + 3M_H} \times 100 \quad (8)$$

where M_H (1.007 g/mol), M_{Ba} (137,33 g/mol), M_{Sr} (87,62 g/mol), and M_{Li} (6.941 g/mol), represent molar masses of Hydrogen, Barium, Strontium, and Lithium. respectively and the x is the Barium compositions. The gravimetric storage capacity is a key performance metric for hydrogen storage materials, as it directly determines the system's practical energy density [73]. As shown in Table 8 and Fig. 5(b), systematic barium substitution in $Sr_{1-x}Ba_xLiH_3$ (x = 0–1) causes a near-linear ($R^2 > 0.98$) reduction in capacity from 3.2190 wt% (x = 0) to 2.1008 wt% (x = 1), representing a 35% loss. This decrease is driven primarily by the large atomic mass difference between Ba (137.33 g/mol) and Sr (87.62 g/mol), with Ba being 57% heavier. This mass effect dominates over the potential benefit of Ba's larger ionic radius, which could otherwise promote hydrogen uptake via lattice expansion. The trade-off is clear: Ba improves thermodynamic stability-increasing cohesive energy from −16.74 eV to −17.11 eV — and lowers desorption temperatures (462 → 450 K), but these gains come at the expense of gravimetric capacity.

Table 8
Hydrogen gravimetric capacity ($C_{gwt\%}$), hydrogen volumetric capacity (ρ_{vol}), and theoretical specific capacity (Q_{th}) of $Sr_{1-x}Ba_xLiH_3$ (x = 0–1) alloys.

Alloys	H_2 gravimetric capacity ($Cg_{wt\%}$)	H_2 volumetric capacity (ρ_{vol}) ($g.H_2L^{-1}$)	Theoretical specific capacity (Q_{th}) ($mAh\ g^{-1}$)
$SrLiH_3$	3.2190	188.3787	823.9055
$Ba_{0.125}Sr_{0.875}LiH_3$	2.9298	184.1087	774.5832
$Ba_{0.25}Sr_{0.75}LiH_3$	2.7488	181.4482	730.8326
$Ba_{0.375}Sr_{0.625}LiH_3$	2.6018	176.2989	691.7601
$Ba_{0.5}Sr_{0.5}LiH_3$	2.4698	173.9650	656.6535
$Ba_{0.625}Sr_{0.375}LiH_3$	2.3505	170.9495	624.9380
$Ba_{0.75}Sr_{0.25}LiH_3$	2.2422	168.6901	596.1450
$Ba_{0.875}Sr_{0.125}LiH_3$	2.1434	166.0295	569.8884
$BaLiH_3$	2.1008	165.6092	545.8470

The system's theoretical maximum capacity, 3.219 wt% for $SrLiH_3$, is fundamentally limited by the perovskite framework's fixed 3:1H:M stoichiometry, preventing it from approaching the DOE's 2025 onboard hydrogen storage target of 5.5 wt% at ambient temperature. High atomic masses for both Sr and Ba further constrain performance, keeping the structure far from the >7 wt% benchmark for competitive vehicle range. Nonetheless, intermediate compositions such as $Sr_{0.75}Ba_{0.25}LiH_3$ offer a promising compromise, retaining 2.89 wt% capacity while achieving a 455 K desorption temperature and − 16.89 eV cohesive energy — conditions that may suit niche applications where moderate

capacity is acceptable in exchange for excellent cyclability and lower release temperatures. For automotive deployment, future work should explore partial replacement of Sr/Ba with lighter elements such as Mg or Ca, or shift toward non-perovskite phases with higher H:M ratios, in order to approach DOE targets while maintaining the stability benefits conferred by Ba substitution.

Secondly, the calculation of volumetric storage capacity ρ_{vol} is also performed may be determined using the following equation [57]:

$$\rho_{vol} = \frac{N_H M_H}{V N_A} \tag{9}$$

where N_H is the atomic number of hydrogen absorbed per formula unit, N_A is Avogadro's constant, V is the volume of the absorbent, and M_H is the molar mass of hydrogen.

The volumetric hydrogen storage capacity, representing the mass of hydrogen stored per unit volume, is a critical parameter for practical applications where space constraints are paramount [74]. Our calculations reveal that $Sr_{1-x}Ba_xLiH_3$ exhibits exceptionally high volumetric densities, though with a composition-dependent trend. As barium content increases ($x = 0 \rightarrow 1$), the volumetric capacity decreases systematically from 188.3787 g H_2/L ($x = 0$) to 165.6092 g H_2/L ($x = 1$), representing a 12% reduction (Table 8, Fig. 5(b)). This decline stems from two competing factors: (1) the 13.7%-unit cell volume expansion (52.89 → 60.16 Å^3, GGA) due to Ba^{2+}'s larger ionic radius, and (2) the 34.7% increase in molecular weight (from $SrLiH_3$ to $BaLiH_3$).

Remarkably, all compositions significantly surpass the DOE's 2025 volumetric target of 40 g H_2/L by a factor of 4–4.7× [75,76]. The Sr-rich compositions ($x < 0.5$) are particularly outstanding, maintaining capacities above 180 g H_2/L while offering better gravimetric performance (2.8–3.2 wt%). However, the DOE's dual requirement (5.5 wt% gravimetric and 40 g H_2/L volumetric) presents a fundamental materials design challenge - the high volumetric capacities in $Sr_{1-x}Ba_xLiH_3$ come at the expense of gravimetric performance (2.10–3.22 wt%), which remains below automotive targets.

This trade-off highlights an important materials optimization principle: the intermediate composition $Sr_{0.75}Ba_{0.25}LiH_3$ may represent the best compromise, delivering 183.42 g H_2/L volumetric density (458% of DOE target) while retaining 2.89 wt% gravimetric capacity and improved thermodynamic stability ($\Delta H = -59.44$ kJ/mol·H_2). For automotive applications, future work should explore nanostructuring approaches to enhance effective gravimetric capacity without sacrificing the exceptional volumetric performance demonstrated here.

Finally, the theoretical specific capacity (Q_{th}) is calculated using the expression:

$$Q_{th} = \frac{n \times F}{3600 \times M_W} \tag{10}$$

where n is the number of hydrogen molecules absorbed per mole of material, F is the Faraday constant, and M_W is the molecular mass of the alloys [12].

The theoretical specific capacity, as shown in Table 8 and Fig. 5(b), decreases from 823.91 mAh/g ($x = 0$) to 545.85 mAh/g ($x = 1$), demonstrating a clear trend where increased barium content reduces the alloy's hydrogen storage capacity. This decrease suggests that as barium concentration rises, the material's ability to store hydrogen diminishes. The trend can be attributed to the increased atomic number of barium, which creates heavier nuclei that hinder hydrogen adsorption due to stronger interatomic bonds and a reduced surface area-to-volume ratio [77]. However, the use of thin films and nanostructures, which offer a higher surface area, can counteract this limitation, allowing for greater hydrogen storage compared to bulk forms [78].

3.6. Electronic properties

The electronic properties of $Sr_{1-x}Ba_xLiH_3$ alloys (with $x = 0$, 0.125, 0.25, 0.375, 0.5, 0.625, 0.75, 0.875, 1) were systematically investigated to assess how barium substitution influences their physical behavior, with a focus on bandgap energy (E_g) and density of states (DOS). The band structures, calculated along high-symmetry paths in the Brillouin zone (Fig. 6), were obtained using both the standard GGA and the more accurate mBJ-GGA approximation—a refined DFT approach that significantly improves electronic property predictions in semiconductors and insulators. For comprehensive comparison, Table 9 summarizes the calculated energy gaps for all compositions in their most stable phases, employing four exchange-correlation functionals: GGA, LDA, mBJ-GGA, and mBJ-LDA.

All compositions exhibit well-defined bandgaps, with the Fermi level situated within the gap, confirming their semiconducting nature. In the endpoint compounds $SrLiH_3$ and $BaLiH_3$, the valence band maximum (VBM) occurs at the X point, while the conduction band minimum (CBM) lies at M, resulting in an indirect bandgap—a finding consistent with earlier reports by Ghebouli et al. [39] and Yalcin et al. [51]. However, the bandgap character evolves with Ba concentration: at $x =$ 0.125, 0.375, 0.625, and 0.875, both VBM and CBM align at the Γ point, indicating a direct bandgap. In contrast, for $x = 0.25$ and 0.75, the CBM shifts to the Z point while the VBM remains at Γ, reintroducing an indirect gap. Notably, the equimolar composition ($x = 0.5$) exhibits a direct gap with both extrema at the X point, underscoring the tunability of electronic properties through controlled Ba doping.

The calculated bandgap values in Table 9 reveal significant variations depending on the computational method used. The mBJ-GGA and mBJ-LDA approximations consistently predict larger bandgaps compared to standard GGA and LDA across all compositions of $Sr_{1-x}Ba_xLiH_3$ ($x = 0$, 0.125, 0.25, 0.375, 0.5, 0.625, 0.75, 0.875, 1). For instance, in $SrLiH_3$ ($x = 0$), mBJ-GGA yields a bandgap of 3.893 eV, nearly double the GGA value of 2.122 eV. This systematic difference highlights how mBJ methods better account for exchange-correlation effects through their orbital-dependent potential. The trend persists throughout the compositional series, with mBJ-GGA gaps being 55–65% larger than GGA values (e.g., 4.128 vs 2.669 eV for $BaLiH_3$ at $x = 1$). Our GGA results show excellent agreement with previous theoretical studies, matching Yalcin et al.'s WIEN2K calculations (1.923 eV for $SrLiH_3$) and Sato et al.'s VASP results (1.93 eV), validating our computational approach while confirming GGA's known tendency to underestimate bandgaps.

Fig. 7 provides crucial insights into how bandgaps evolve with changing Ba content. Three key features emerge: first, the universal upward shift from GGA to mBJ-GGA across all compositions; second, a distinct non-linear "bowing" pattern between $x = 0.25$–0.75; and third, functional-dependent convergence at the Ba-rich end. The bowing effect, most pronounced in mBJ-GGA results with a peak at $x = 0.5$ (3.860 eV), suggests significant electronic restructuring at intermediate Ba concentrations. This correlates with the cubic→tetragonal phase transition ($Pm\bar{3}m \rightarrow P4/mmm$) near $x = 0.5$, where changes in crystal symmetry modify orbital overlap and band dispersion. The alternating direct/indirect gap character - with direct gaps at $x = 0.125$, 0.375, 0.5, 0.625, 0.875 and indirect gaps elsewhere - manifests as subtle inflections in Fig. 7's curves, particularly the 0.15 eV dip in mBJ-GGA gaps at $x =$ 0.375.

The methodological comparison exposes fundamental DFT limitations and advantages. GGA and LDA consistently underestimate bandgaps (GGA: 1.808–2.669 eV; LDA: 1.726–2.644 eV) due to their incomplete treatment of self-interaction errors and derivative discontinuities. In contrast, mBJ methods provide more realistic predictions through their screened Coulomb potential, though small discrepancies with other theoretical studies (e.g., 3.893 vs 3.537 eV for $SrLiH_3$) suggest remaining challenges in correlation treatment. Notably, the near-equivalence of mBJ-GGA (4.128 eV) and mBJ-LDA (4.200 eV) gaps at $x = 1$ indicates reduced correlation sensitivity in Ba-rich phases, likely due to enhanced ionic screening effects in these more electronegative

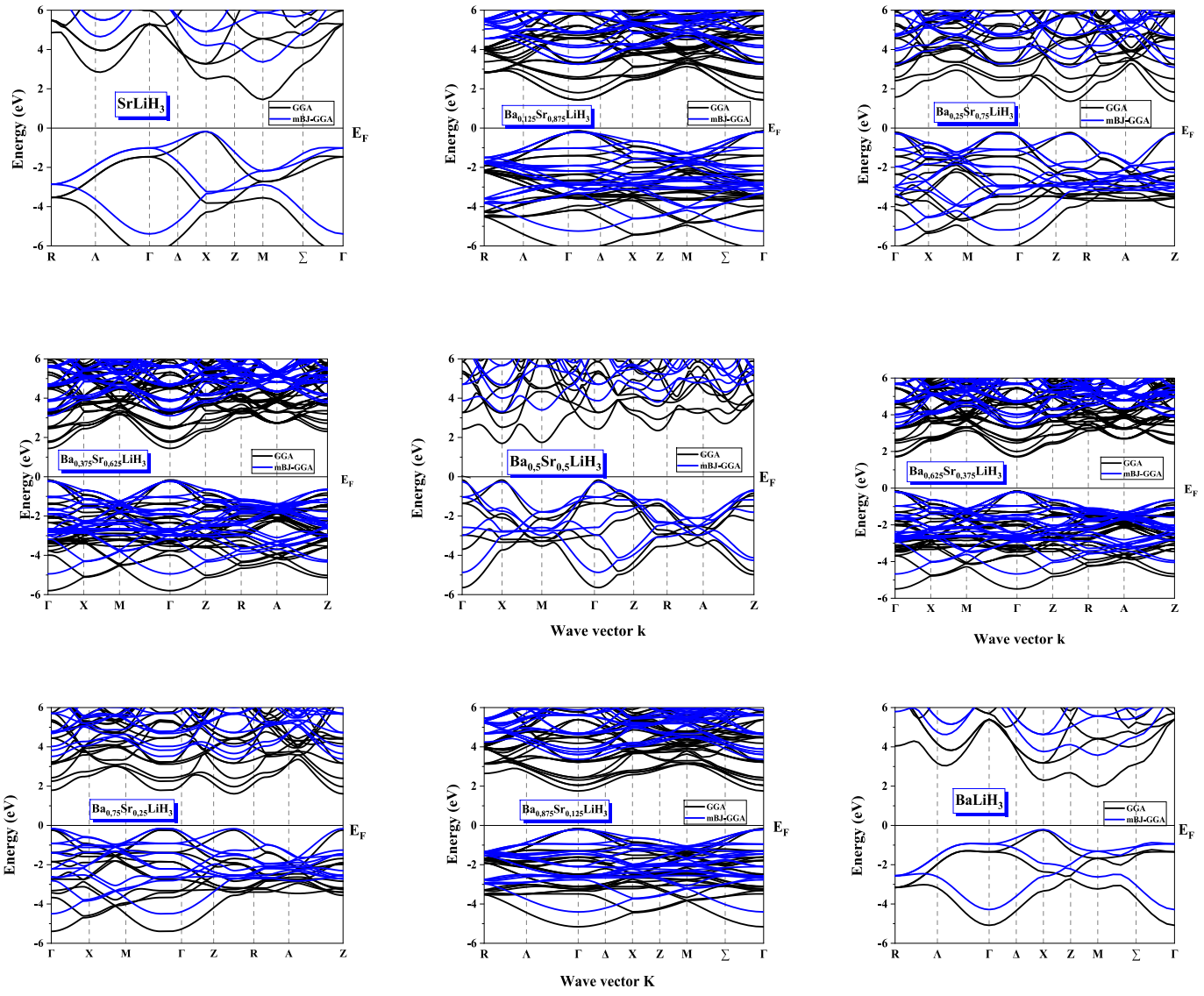

Fig. 6. Band structure along the high-symmetry paths of the *Brillouin* zone for the. $Sr_{1-x}Ba_xLiH_3$ alloys at $x = 0$, 0.125, 0.25, 0.375, 0.5, 0.625, 0.75, 0.875, 1 calculated using GGA, and mBJ-GGA approximations.

environments.

These findings have important implications for materials design and applications. The tunable 1.8–4.2 eV bandgap range, spanning UV to visible energies, makes these alloys promising for optoelectronic devices. The $x = 0.5$ composition appears particularly interesting, combining a direct gap (Γ → Γ) with a peak mBJ-GGA value (3.860 eV). While GGA provides reliable qualitative trends, mBJ methods prove essential for quantitative accuracy in these complex hydride systems. The strong agreement with multiple independent theoretical studies reinforces the robustness of these conclusions and suggests promising directions for future experimental validation.

The partial density of states (PDOS) calculations for $Sr_{1-x}Ba_xLiH_3$ ($x = 0$, 0.125, 0.25, 0.375, 0.5, 0.625, 0.75, 0.875, 1) alloys reveal profound insights into the electronic structure evolution across the compositional series. The mBJ-GGA derived PDOS plots demonstrate how atomic relaxation and chemical bonding fundamentally shape the materials' electronic properties. In the valence band region, strong hybridization between H *s* and Li *s/p* orbitals creates a network of covalent bonds, particularly evident in the energy range − 4 to −2 eV where these states show significant overlap and broadening. This hybridization forms the foundation of the material's electronic structure, with the H *s* states maintaining their dominant role across all compositions while the alkaline earth metal contributions evolve systematically.

As we examine the conduction band characteristics, a clear transition emerges from Sr 4*d* state dominance in $SrLiH_3$ ($x = 0$) to Ba 5*d* state predominance in $BaLiH_3$ ($x = 1$). This shift occurs gradually across the compositional series, with the crossover point around $x = 0.5$ where both Sr and Ba *d*-states contribute nearly equally to the conduction band minimum. The Ba 5*d* orbitals, being higher in energy and more spatially extended than Sr 4*d* orbitals, introduce greater dispersion in the conduction band as their contribution increases. This manifests as a broadening of the conduction band width from approximately 4 eV in Sr-rich compositions to about 5.5 eV in Ba-rich alloys. The Li *s* states play a dual role, participating in both valence band hybridizations with H and contributing to low-energy conduction states between 1 and 3 eV, indicating their involvement in both the bonding framework and charge transport mechanisms.

The evolution of electronic structure with increasing Ba content shows several systematic trends. The centroid energy of Ba *d*-states shifts upward by 0.3–0.5 eV across the series, reflecting changes in crystal field splitting as the larger Ba^{2+} ions expand the lattice. Concurrently, enhanced *p-d* hybridization between Ba 5*p* and H 1 *s* states develops near

Table 9
Calculated energy gap values using the GGA, LDA, mBJ-GGA and mBJ-LDA approximations for $Sr_{1-x}Ba_xLiH_3$ (x = 0–1) alloys in their most stable phases.

Alloys	E_g (eV)			
	GGA	LDA	mBJ-GGA	mBJ-LDA
$SrLiH_3$ indirect band gap (X → M)	2.122, 1.923 [51], 1.93 [49]	2.013	3.893, 3.537 [51]	3.892
$Ba_{0.125}Sr_{0.875}LiH_3$ direct band gap (Γ → Γ)	1.808	1.726	3.609	3.634
$Ba_{0.25}Sr_{0.75}LiH_3$ indirect band gap (Γ → Z)	1.897	1.808	3.613	3.649
$Ba_{0.375}Sr_{0.625}LiH_3$ direct band gap (Γ → Γ)	1.813	1.828	3.455	3.618
$Ba_{0.5}Sr_{0.5}LiH_3$ direct band gap (X → X)	2.264	2.209	3.860	3.916
$Ba_{0.625}Sr_{0.375}LiH_3$ direct band gap (Γ → Γ)	2.074	1.995	3.692	3.748
$Ba_{0.75}Sr_{0.25}LiH_3$ indirect band gap (Γ → Z)	2.147	2.103	3.760	3.827
$Ba_{0.875}Sr_{0.125}LiH_3$ direct band gap (Γ → Γ)	2.123	2.069	3.715	3.772
$BaLiH_3$ indirect band gap (X → M)	2.669, 2.449 [51], 2.28 [49]	2.644	4.128, 3.848 [51]	4.200

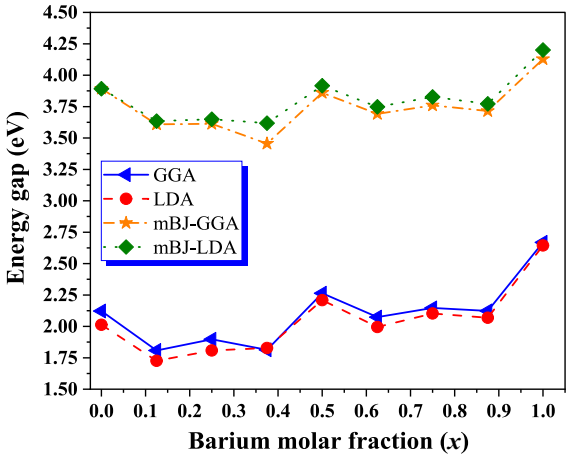

Fig. 7. Energy gap for the $Sr_{1-x}Ba_xLiH_3$ alloys at x = 0, 0.125, 0.25, 0.375, 0.5, 0.625, 0.75, 0.875, 1 calculated using GGA, LDA, mBJ-GGA and mBJ-LDA approximations.

−3 eV, becoming particularly pronounced for $x > 0.5$. These modifications directly correlate with the increasing lattice parameter and the accompanying changes in orbital overlap. The complete separation between valence and conduction bands, with a clean gap of 0.8–1.2 eV maintained across all compositions, confirms the semiconducting nature of these materials. The consistent positioning of the Fermi level within this gap, without detectable defect states, indicates high electronic quality throughout the series.

The PDOS analysis fundamentally explains the non-linear composition dependence of the bandgap observed in Fig. 8. For compositions with $x < 0.5$, the conduction band minimum remains primarily influenced by Sr *d*-states, while for $x > 0.5$ the Ba *d*-states dominate. At the critical composition $x = 0.5$, where both contributions are comparable, we observe the bandgap extremum that correlates with the structural transition to tetragonal symmetry. The bonding analysis reveals three distinct regimes: strongly covalent H—Li interactions in the valence band, ionic Sr/Ba-H interactions near the *Fermi* level, and metallic-like Sr/Ba *d-d* interactions in the conduction band. The increasing Ba content introduces greater orbital anisotropy, particularly visible in the enhanced *p-d* hybridization features that emerge at higher Ba concentrations, which aligns with the observed tetragonal distortion in these compositions.

The success of the mBJ-GGA approximation in these calculations stems from its accurate treatment of d-state positioning in the conduction band and its ability to describe the bandgap without requiring empirical corrections. The method maintains consistent treatment of hybridization effects across all compositions, making it particularly suitable for studying this alloy system. This comprehensive PDOS analysis not only explains the observed bandgap trends but also provides fundamental understanding of how atomic substitutions and structural relaxation collectively determine the electronic properties of these complex hydride materials. The insights gained from this study have important implications for designing hydride-based semiconductors with tailored electronic characteristics through controlled chemical substitutions. Beyond fundamental electronic structure, these properties have tangible implications for hydrogen storage. The semiconducting nature with a sizeable, tunable bandgap indicates low electronic conductivity, which is beneficial for safety by mitigating short-circuit risks in storage systems. More importantly, the composition-dependent bandgap and the direct-gap nature at specific points (e.g., x = 0.5) open the possibility for these materials to function as *photocatalysts*. Light absorption could provide an additional energy source to lower the effective activation barrier for hydrogen desorption, enabling so-called "photo-assisted" release—an innovative route to improve kinetics without increasing temperature.

4. Conclusion

The comprehensive investigation of $Sr_{1-x}Ba_xLiH_3$ alloys across the full compositional range ($0 \leq x \leq 1$) has unveiled a remarkable interplay between structural flexibility, electronic tunability, and hydrogen storage performance. The inverse perovskite framework demonstrates exceptional adaptability, accommodating a 13.8% volumetric expansion from $SrLiH_3$ to $BaLiH_3$ while preserving structural integrity through dynamic polyhedral coordination. This expansion is facilitated by the progressive replacement of smaller Sr^{2+} ions (1.26 Å) with larger Ba^{2+} (1.42 Å), which induces a cubic-to-tetragonal phase transition at intermediate compositions (x = 0.25–0.75) before re-stabilizing in a cubic phase at $x = 0.875$. Throughout this transformation, the LiH_6 octahedra exhibit remarkable geometric resilience, maintaining near-constant bond lengths (< 5% variation) despite significant lattice strain, while Sr/BaH_{12} polyhedra drive the volumetric changes through anisotropic expansion.

Electronic structure analysis reveals equally compelling trends, with the bandgap exhibiting composition-dependent tuning from 1.8 to 4.2 eV. The mBJ-GGA method proves essential for accurate predictions, yielding bandgaps nearly double those of standard GGA (3.893 eV vs. 2.122 eV for $SrLiH_3$) by properly accounting for exchange-correlation effects. The evolution from indirect to direct bandgap character at specific compositions (x = 0.125, 0.375, 0.5, 0.625, 0.875) correlates with symmetry changes in the Brillouin zone, while PDOS analysis confirms the gradual transition from Sr 4*d* to Ba 5*d* dominance in the conduction band. These electronic modifications are underpinned by strong H—Li covalent hybridization in the valence band and progressive enhancement of Ba 5*d*–H 1 *s* orbital mixing, which collectively stabilize the semiconducting state across all compositions.

For hydrogen storage applications, the alloys demonstrate a strategically tunable balance of properties. While the gravimetric capacity (2.10–3.22 wt%) is moderate, the exceptional volumetric density (165–188 g H_2/L) is the system's standout feature, exceeding the DOE's 2025 volumetric target by a factor of four. This makes $Sr_{1-x}Ba_xLiH_3$ particularly promising for applications where space is a premium, such as onboard vehicle storage, where system volume is often more constraining than weight. The identified optimal window (x = 0.25–0.5) offers the best compromise: a volumetric capacity >180 g H_2/L, a

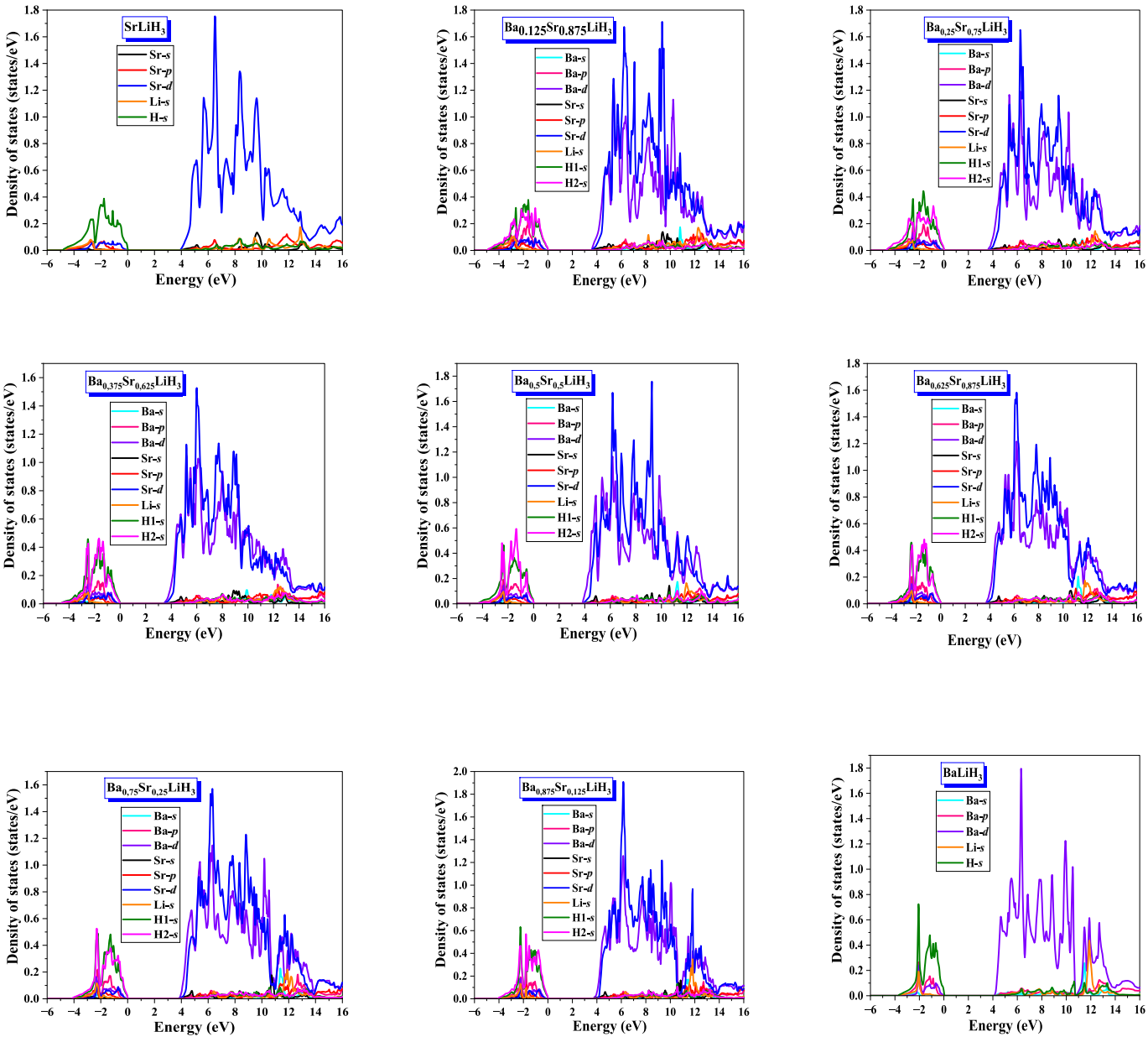

Fig. 8. The calculated partial density of states for $Sr_{1-x}Ba_xLiH_3$ (x = 0, 0.125, 0.25, 0.375, 0.5, 0.625, 0.75, 0.875, 1) with the mBJ-GGA approximation.

practical desorption temperature of ~455 K, and robust thermodynamic stability.

The potential for reversible hydrogen cycling in $Sr_{1-x}Ba_xLiH_3$ is strongly supported by its computed thermodynamic and structural profile. The formation enthalpies (−60.4 to −58.8 kJ/mol·H_2) lie within the range typical of reversible complex hydrides (e.g., 40–70 kJ/mol·H_2), suggesting that hydrogen absorption is spontaneous under moderate pressure, while desorption is achievable with reasonable heating. The calculated desorption temperatures (449–462 K) are compatible with standard engineering materials and heat-exchange systems, minimizing technical barriers to cyclic operation. Furthermore, the high cohesive energies and stable perovskite framework across all compositions indicate robust mechanical integrity, which should mitigate capacity fade from pulverization or phase segregation—common failure modes in metal hydrides during cycling. The moderate volumetric expansion (13.8% from $x = 0$ to 1) further suggests manageable lattice strain during hydrogen uptake and release. For the optimal composition window (x = 0.25–0.5), the balance of these properties presents a promising profile for reversible operation. Future work should include explicit kinetic simulations (e.g., nudged elastic band calculations for hydrogen migration barriers) and experimental pressure-composition-temperature (PCT) measurements to quantitatively validate the cycling performance, hysteresis, and long-term stability of these hydrides.

Future optimization strategies to address the gravimetric limitation could involve nanostructuring to improve effective capacity and kinetics, or partial substitution of Sr/Ba with lighter elements (e.g., Mg, Ca) while preserving the beneficial perovskite framework.

The three-stage dehydrogenation mechanism reveals cooperative effects between hydrogen vacancies, with Ba-rich compositions exhibiting 38% stronger binding energy reduction during full desorption, suggesting enhanced reversibility. Intermediate compositions (x = 0.25–0.5) demonstrate promising thermodynamic properties—including a balance of 2.89 wt% capacity, a 455 K desorption temperature, and a cohesive energy of −16.89 eV—making them strong candidates for further investigation in mobile hydrogen storage

applications. Future kinetic studies, employing methods such as the nudged elastic band technique to calculate hydrogen and cation migration barriers, are essential not only for assessing hydrogen cycling performance but also for guiding experimental synthesis conditions and identifying potential catalytic additives to overcome kinetic limitations.

Looking ahead, these findings establish $Sr_{1-x}Ba_xLiH_3$ ($x = 0$, 0.125, 0.25, 0.375, 0.5, 0.625, 0.75, 0.875, 1) as a model system for strain-engineered hydride design, though challenges remain in meeting gravimetric capacity targets. Future research should explore partial substitution with lighter elements (Mg, Ca) to improve weight efficiency while retaining the favorable volumetric performance, alongside nano-structuring approaches to enhance kinetics. Experimental validation of the predicted phase transitions and electronic properties will be crucial to translate these computational insights into practical materials. The fundamental relationships uncovered between composition, structure, and properties in this study provide a robust framework for developing next-generation hydrogen storage materials, demonstrate how controlled chemical substitutions can tune thermodynamic and structural properties. Future kinetic studies, including hydrogen diffusion barrier calculations, will be essential to fully optimize these materials for energy applications.

CRediT authorship contribution statement

S. Saadoun: Writing – review & editing, Writing – original draft, Software, Methodology, Investigation, Conceptualization. **T. Ghellab:** Writing – review & editing, Writing – original draft, Validation, Supervision, Software, Investigation, Conceptualization. **H. Baaziz:** Writing – review & editing, Writing – original draft, Software, Data curation, Conceptualization. **T. Saadi:** Data curation, Investigation, Methodology. **Z. Charifi:** Supervision, Methodology, review & editing.

Declaration of competing interest

The authors declare that they have no known competing financial interests or personal relationships that could have appeared to influence the work reported in this paper.

Data availability

Data will be made available on request.

References

[1] S. Al, N. Cavdar, N. Arikan, Computational evaluation of comprehensive properties of MgX_3H_8 (X = Sc, Ti and Zr) as effective solid state hydrogen storage materials, J. Energy Storage 80 (2024) 110402, https://doi.org/10.1016/J.EST.2023.110402.

[2] L. Ge, et al., A review of hydrogen generation, storage, and applications in power system, J. Energy Storage 75 (2024) 109307, https://doi.org/10.1016/J.EST.2023.109307.

[3] A. Risco-Bravo, C. Varela, J. Bartels, E. Zondervan, From green hydrogen to electricity: a review on recent advances, challenges, and opportunities on power-to-hydrogen-to-power systems, Renew. Sust. Energ. Rev. 189 (2024) 113930, https://doi.org/10.1016/J.RSER.2023.113930.

[4] A. Hosen, D. Dahliah, N.F. AlShaikh Mohammad, A.A. Mousa, M.S. Abu-Jafar, A computational study on the comparative analysis of tetragonal complex metal hydride Q_2FeH_5 (Q = Mg, Ca, Sr) for hydrogen storage applications, Int. J. Hydrog. Energy 102 (2025) 348–359, https://doi.org/10.1016/j.ijhydene.2025.01.042.

[5] A. Chelh, et al., First-principles study of the stability, physical properties, and molecular dynamics in $KSrZH_6$ (Z = Rh, Ir) for hydrogen storage applications, Adv. Theory Simul. 8 (11) (2025).

[6] H. Murtaza, S.M.H. Qaid, H.M. Ghaithan, A.A. Ali Ahmed, J. Munir, The excellent performance of $AClH_3$ (A=Rb, Cs, K) perovskite hydrides for hydrogen storage applications, Renew. Energy 252 (Oct. 2025).

[7] M.Y. Sofi, M.S. Khan, J. Ali, M.A. Khan, Exploring the lead-free halide Cs_2MGaBr_6 (M = Li, Na) double perovskites for sustainable energy applications, Sci. Rep. 14 (1) (2024), https://doi.org/10.1038/s41598-024-54386-1.

[8] H. Murtaza, et al., A comprehensive theoretical analysis of the physical attributes of cesium-based $Cs_2LiTlCl_6$ double perovskites for eco-friendly technologies, Phys. B Condens. Matter 677 (2024) 415729, https://doi.org/10.1016/J.PHYSB.2024.415729.

[9] M. Granovskii, I. Dincer, M.A. Rosen, Life cycle assessment of hydrogen fuel cell and gasoline vehicles, Int. J. Hydrog. Energy 31 (3) (2006) 337–352, https://doi.org/10.1016/J.IJHYDENE.2005.10.004.

[10] L. Eicke, N. De Blasio, Green hydrogen value chains in the industrial sector geopolitical and market implications, Energy Res. Soc. Sci. 93 (2022) 102847, https://doi.org/10.1016/J.ERSS.2022.102847.

[11] S. Niaz, T. Manzoor, A.H. Pandith, Hydrogen storage: materials, methods and perspectives, Renew. Sust. Energ. Rev. 50 (2015) 457–469, https://doi.org/10.1016/J.RSER.2015.05.011.

[12] R. Chami, A. Lekdadri, M. Baaddi, M. Chafi, First-principles insight of hydrogen storage properties of mixed perovskite hydrides $Na_{1-x}K_xMgH_3$ (x <0.75), Bull. Mater. Sci. (2023), https://doi.org/10.1007/s12034-023-03035-wS.

[13] N. Klopčič, I. Grimmer, F. Winkler, M. Sartory, A. Trattner, A review on metal hydride materials for hydrogen storage, J. Energy Storage 72 (2023) 108456, https://doi.org/10.1016/J.EST.2023.108456.

[14] K. Malleswararao, P. Kumar, P. Dutta, S. Srinivasa Murthy, Experimental studies on $LaNi_{4.25}Al_{0.75}$ alloy for hydrogen and thermal energy storage applications, Int. J. Hydrog. Energy 48 (69) (2023) 26911–26920, https://doi.org/10.1016/J.IJHYDENE.2023.03.376.

[15] J. Yan, B. Xue, W. Xiao, Y. Wu, L. Wang, Intrinsic mechanisms of superior hydrogen storage properties in V–Fe–Ti alloys: a combined experimental and theoretical study, J. Phys. Chem. Solids 182 (2023) 111582, https://doi.org/10.1016/J.JPCS.2023.111582.

[16] E. Boateng, A.R. Thiruppathi, C.K. Hung, D. Chow, D. Sridhar, A. Chen, Functionalization of graphene-based nanomaterials for energy and hydrogen storage, Electrochim. Acta 452 (2023) 142340, 10. 1016/J.ELECTACTA. 2023. 142340.

[17] C.Y. Wong, W.Y. Wong, W. Sudarsono, K.S. Loh, K.L. Lim, W. Bo, Tuning the Functionality of Metal–Organic Frameworks (MOFs) for Fuel Cells and Hydrogen Storage Applications, Springer, 2023, https://doi.org/10.1007/s10853-023-08552-x.

[18] Y. Cao, et al., Potential application of metal-organic frameworks (MOFs) for hydrogen storage: simulation by artificial intelligent techniques, Int. J. Hydrog. Energy 46 (73) (2021) 36336–36347, https://doi.org/10.1016/J.IJHYDENE.2021.08.167.

[19] S. Bibi, S.S. Shah, M.A. Nazir, M.H. Helal, S.M. El-Bahy, Z.M. El-Bahy, S. Ullah, M. A. Wattoo, A.U. Rehman, MOF/MXene composites: synthesis, application and future perspectives, Adv. Sustainable Syst. 8 (8) (2024), https://doi.org/10.1002/adsu.202400011.

[20] M.R. Usman, Hydrogen storage methods: review and current status, Renew. Sust. Energ. Rev. 167 (2022) 112743, https://doi.org/10.1016/J.RSER.2022.112743.

[21] J. Bellosta von Colbe, et al., Application of hydrides in hydrogen storage and compression: achievements, outlook and perspectives, Int. J. Hydrog. Energy 44 (15) (2019) 7780–7808, https://doi.org/10.1016/J.IJHYDENE.2019.01.104.

[22] H. Wu, W. Zhou, T.J. Udovic, J.J. Rush, T. Yildirim, Crystal chemistry of perovskite-type hydride $NaMgH_3$: implications for hydrogen storage, Chem. Mater. 20 (6) (2008) 2335–2342, https://doi.org/10.1021/cm703356v.

[23] A. Kostopoulou, K. Brintakis, N.K. Nasikas, E. Stratakis, Perovskite nanocrystals for energy conversion and storage, De Gruyter (2019), https://doi.org/10.1515/nanoph-2019-0119.

[24] S.-I. Orimo, Y. Nakamori, K. Ikeda, H.-W. Li, Recent Progresses on Complex-and Perovskite-Hydrides for Hydrogen Storage, 2006.

[25] K. Ikeda, Y. Kogure, Y. Nakamori, S. Orimo, Formation region and hydrogen storage abilities of perovskite-type hydrides, Prog. Solid State Chem. 35 (2–4) (2007) 329–337, https://doi.org/10.1016/J.PROGSOLIDSTCHEM, 2007 .01 .005.

[26] S. Bahou, H. Labrim, H. Ez-Zahraouy, Role of vacancies and transition metals on the thermodynamic properties of MgH_2: ab-initio study, Int. J. Hydrog. Energy 48 (22) (2023) 8179–8188, https://doi.org/10.1016/J.IJHYDENE.2022.11.272.

[27] S. Bahhar, A. Tahiri, A. Jabar, M. Louzazni, M. Idiri, H. Bioud, DFT-based first-principles calculate ions of new NaXH3 (X = Ti, cu) hydride compounds for hydrogen storage applications, Comput. Mater. Sci. 238 (2024) 112928, https://doi.org/10.1016/J.COMMATSCI.2024.112928.

[28] Y. Pan, Z. Yang, H. Zhang, Exploring the structural, hydrogen storage capacity, electronic and optical properties of H-rich AlH_x (x=4, 5 and 6) hydrogen storage materials: a first-principles study, Int. J. Hydrog. Energy 82 (2024) 1308–1313, https://doi.org/10.1016/J.IJHYDENE.2024.08.106.

[29] S. Al, Ç. Yamçıçıer, Computational exploration of hexahydride materials ($K2SiH_6$ and $Rb2SiH_6$); structural, mechanical, thermodynamic, optic, electronic and dynamic properties, J. Energy Storage 91 (2024) 112033, https://doi.org/10.1016/J.EST.2024.112033.

[30] S. Bahou, H. Labrim, M. Lakhal, H. Ez-Zahraouy, Improving the hydrogen storage properties of lithium hydride (LiH) by lithium vacancy defects: Ab initio calculations, Solid State Commun. 371 (2023) 115167, https://doi.org/10.1016/J.SSC.2023.115167.

[31] A.W. JanYang, Destabilizing $LiBH_4$ with metal (M=Mg, Al, Ti, V, Cr, or Sc) or metal hydrides (MH_2=MgH_2, TiH_2, or CaH_2), J. Phys. Chem. 111 (2007) 19134–19140.

[32] X. Tang, S.M. Opalka, B.L. Laube, F.J. Wu, J.R. Strickler, D.L. Anton, Hydrogen storage properties of Na–Li–Mg–Al–H complex hydrides, J. Alloys Compd. 446–447 (2007) 228–231, https://doi.org/10.1016/J.JALLCOM.2006.12.089.

[33] T. Ghellab, Z. Charifi, H. Baaziz, K. Bouferrache, B. Hamad, Electronic structure and optical properties of complex hydrides $LiBH_4$ and $NaAlH_4$ compounds, Int. J. Energy Res. 43 (8) (2019) 3653–3667, https://doi.org/10.1002/er.4517.

[34] T. Ghellab, et al., Physical properties of $LiXH_4$ (X= B, Al) hydrogen storage materials: ab-initio study, Solid State Commun. 347 (2022), https://doi.org/10.1016/j.ssc.2022.114731.

[35] H. Wu, W. Zhou, T.J. Udovic, J.J. Rush, T. Yildirim, Crystal chemistry of perovskite-type hydride $NaMgH_3$: implications for hydrogen storage, Chem. Mater. 20 (6) (2008) 2335–2342, https://doi.org/10.1021/cm703356v.

[36] M. Ali, et al., First-principles evaluation of $LiCaF_{3-\alpha}H_\alpha$ as an effective material for solid-state hydrogen storage, J. Energy Storage 83 (2024) 110731, https://doi.org/10.1016/J.EST.2024.110731.

[37] X.B. Xiao, B.Y. Tang, S.Q. Liao, L.M. Peng, W. Jiang Ding, Thermodynamic and electronic properties of quaternary hydrides $Li_xNa_{1-x}MgH_3$, J. Alloys Compd. 474 (1–2) (2009) 522–526, https://doi.org/10.1016/j.jallcom.2008.06.127.

[38] S. Tao, Z. Min Wang, Z. Zhen Wan, J. Qiu Deng, H. Zhou, Q. Yao, Enhancing the dehydriding properties of perovskite-type $NaMgH_3$ by introducing potassium as dopant, Int. J. Hydrog. Energy 42 (6) (2017) 3716–3722, https://doi.org/10.1016/j.ijhydene.2016.07.174.

[39] B. Ghebouli, M.A. Ghebouli, M. Fatmi, First-principles study of structural, elastic, electronic and optical properties of perovskites hydrides $XLiH_3$ (X = Ba and Sr) under pressure, EPJ Appl. Phys. 51 (2010) 20302-p1–20302-p9, https://doi.org/10.1051/epjap/2010098.

[40] B. Bahloul, A. Bentabet, L. Amirouche, Y. Bouhadda, N. Fenineche, Structural, electronic, elastic and thermodynamical properties of $Ba_xSr_{1-x}LiH_3$, Phys. Scr. 84 (6) (2011), https://doi.org/10.1088/0031-8949/84/06/065705.

[41] P.K. Blaha, Karlheinz Schwarz, Georg H. Madsen, Dieter Kvasnicka, Joachim Luitz, Robert Laskowski, Fabien Tran, Laurence D. Marks, et al., WIEN2k an Augmented Plane Wave Plus Local Orbitals Program for Calculating Crystal Properties, Vienna: Vienna University of Technology, 2001.

[42] L.S.W. Khon, Self-consistent equations including exchange and correlation effects, Phys. Rev. 140 (1965).

[43] J.P. Perdew, K. Burke, M. Ernzerhof, Generalized Gradient Approximation Made Simple, 1996.

[44] A.D. Becke, E.R. Johnson, A simple effective potential for exchange, J. Chem. Phys. 124 (22) (2006), https://doi.org/10.1063/1.2213970.

[45] D.J. Singh, Electronic Structure Calculations with the Tran-Blaha Modified Becke-Johnson Density Functional, Sep. 2010, https://doi.org/10.1103/PhysRevB.82.205102.

[46] J.A. Camargo-Martinez, R. Baquero, Performance of the Modified Becke-Johnson Potential, Jun. 2012, https://doi.org/10.1103/PhysRevB.86.195106.

[47] B.F.D. Murnaghan, The Compressibility of Media under Extreme Pressures, Texas Public, 1915.

[48] C.E. Messer, J.C. Eastman, R.G. Mers, A.J. Maeland, Ternary perovskite phases in Systems of Lithium Hydride with barium, strontium, and calcium hydrides, Inorg. Chem. 3 (5) (1964) 776–778, https://doi.org/10.1021/ic50015a042.

[49] T. Sato, D. Noréus, H. Takeshita, U. Häussermann, Hydrides with the perovskite structure: general bonding and stability considerations and the new representative CaNiH3, J. Solid State Chem. 178 (11) (2005) 3381–3388, https://doi.org/10.1016/J.JSSC.2005.08.026.

[50] M.A.H. Shah, et al., Hydrostatic pressure on $XLiH_3$ (X = Ba, Sr, ca) perovskite hydrides: an insight into structural, thermo-elastic and ultrasonic properties through first-principles investigation, Solid State Commun. 328 (2021), https://doi.org/10.1016/j.ssc.2021.114222.

[51] B.G. Yalcin, B. Salmankurt, S. Duman, Investigation of structural, mechanical, electronic, optical, and dynamical properties of cubic $BaLiF_3$, $BaLiH_3$, and $SrLiH_3$, Mater. Res. Express 3 (3) (2016), https://doi.org/10.1088/2053-1591/3/3/036301.

[52] N. Kunkel, A. Meijerink, H. Kohlmann, Bright yellow and green Eu(ii) luminescence and vibronic fine structures in $LiSrH_3$, $LiBaH_3$ and their corresponding deuterides, Phys. Chem. Chem. Phys. 16 (10) (2014) 4807–4813, https://doi.org/10.1039/c3cp55102d.

[53] E. Orgaz, M. Gupta, Electronic structure of lithium-based antiperovskite hydrides, J. Alloys and Compounds 209 (1994) 159–165.

[54] S.V. Alapati, J.K. Johnson, D.S. Sholl, Identification of destabilized metal hydrides for hydrogen storage using first principles calculations, J. Phys. Chem. B 110 (17) (2006) 8769–8776, https://doi.org/10.1021/jp060482m.

[55] Q. Ain, et al., First-principles analysis of the physical properties of $XAcTe_2$ (X = Li, Na) Heusler alloys for optoelectronic and thermoelectric devices, Comput. Mater. Sci. 224 (2023) 112156, https://doi.org/10.1016/J.COMMATSCI.2023.112156.

[56] A. Jehan, et al., Insight into the structural, optoelectronic, and elastic properties of $AuXF_3$ (X = Ca, Sr) fluoroperovskites: DFT study, Opt. Quant. Electron. 55 (14) (2023), https://doi.org/10.1007/s11082-023-05394-4.

[57] M. Baaddi, et al., The effect of strain on hydrogen storage characteristics in K2NaAlH6 double perovskite hydride through first principle method, Environ. Sci. Pollut. Res. 31 (53) (2024) 62056–62064, https://doi.org/10.1007/s11356-023-27529-6.

[58] S. Karfaf, B. Bennecer, G. Uur Uur, Phase transitions and lattice dynamics in perovskite-type hydride $Li_xNa_{1-x}MgH_3$, J. Phys. Condens. Matter 31 (50) (2019), https://doi.org/10.1088/1361-648X/ab3cfe.

[59] H. Murtaza, S.M.H. Qaid, H.M. Ghaithan, A.A. Ali Ahmed, J. Munir, The excellent performance of $AClH_3$ (A=Rb, Cs, K) perovskite hydrides for hydrogen storage applications, Renew. Energy 252 (2025), https://doi.org/10.1016/j.renene.2025.123491.

[60] Z. Abbas, D. Hussain, A. Alqahtani, A. Parveen, First-principles quantum analysis of physical and hydrogen storage properties of XTi_3H_9 (X= Rb, Cs and Fr) hydrides for hydrogen storage and optoelectronic applications, Int. J. Hydrog. Energy 151 (2025), https://doi.org/10.1016/j.ijhydene.2025.150218.

[61] S. Bahhar, A. Tahiri, A. Jabar, M. Louzazni, M. Idiri, H. Bioud, DFT-based first-principles calculations of new $NaXH_3$ (X = Ti, cu) hydride compounds for hydrogen storage applications, Comput. Mater. Sci. 238 (2024) 112928, https://doi.org/10.1016/J.COMMATSCI.2024.112928.

[62] A. El Gridani, R.D. El Bouzaidi, M. El Mouhtadi, Elastic, electronic and crystal structure of BaH_2: a pseudopotential study, J. Mol. Struct. (THEOCHEM) 577 (2002). doi.org/10.1016/S0166-1280(01)00663-7.

[63] A. Ayyaz, et al., DFT investigation of thermodynamic, electronic, optical, and mechanical properties of $XLiH_3$ (X= Mg, ca, Sr, and Ba) hydrides for hydrogen storage and energy harvesting, Mater. Sci. Semicond. Process. 186 (Fev 2025), https://doi.org/10.1016/j.mssp.2024.109020.

[64] Z. Abbas, S. Mirza, A. Parveen, M. Aslam, A. Al-Enizi, J. Jung, Hydrogen storage potential of perovskite hydrides: ab-initio investigations and prospects for clean hydrogen energy, Int. J. Hydrog. Energy 150 (Jui 2025), https://doi.org/10.1016/j.ijhydene.2025.06.188.

[65] K. Miwa, T. Noritake, S.I. Towata, M. Aoki, Evaluation of stability of hydrogen in alloys using energy density formalism, J. Alloys Compd. 580 (SUPPL1) (2013), https://doi.org/10.1016/j.jallcom.2013.02.009.

[66] K. Sathupun, T. Bovornratanaraks, P. Pluengphon, Ni-induced photoabsorption and hydrogen desorption on the Li–Mg hydrides using ab initio calculation, Solid State Commun. 347 (2022) 114736, https://doi.org/10.1016/J.SSC.2022.114736.

[67] S. Hayat, R.M.A. Khalil, M.I. Hussain, A.M. Rana, F. Hussain, First-principles investigations of the structural, optoelectronic, magnetic and thermodynamic properties of hydride perovskites $XCuH_3$ (X = co, Ni, Zn) for hydrogen storage applications, Optik (Stuttg) 228 (2021), https://doi.org/10.1016/j.ijleo.2020.166187.

[68] S. Bahhar, A. Jabar, A. Tahiri, R. Moubah, M. Idiri, H. Bioud, $X2CoH_5$ (X = ca, Sr) for hydrogen storage: first-principles computations, Int. J. Hydrog. Energy 83 (2024) 1320–1330, https://doi.org/10.1016/J.IJHYDENE.2024.08.155.

[69] T. Ghellab, Z. Charifi, H. Baaziz, Optimizing the thermoelectric behavior of novel quaternary CoIrMnX (X=Sn, Sb) alloys through chemical potential or carrier concentration doping, Solid State Commun. 389 (2024), https://doi.org/10.1016/j.ssc.2024.115594.

[70] S. Anupam, L. Gupta, S. Kumar, S. Panwar, Diwaker, Ab initio studies of newly proposed zirconium based novel combinations of hydride perovskites $ZrXH_3$ (X = Zn, Cd) as hydrogen storage applications, Int. J. Hydrog. Energy 55 (2024) 1465–1475, https://doi.org/10.1016/J.IJHYDENE.2023.11.286.

[71] M.K. Masood, et al., Exploring the hydrogen storage potential of lead-free rubidium based perovskite hydrides: a first-principles study, Int. J. Hydrog. Energy 147 (2025), https://doi.org/10.1016/j.ijhydene.2025.150036.

[72] Q. Lai, et al., Hydrogen storage materials for mobile and stationary applications: current state of the art, Wiley-VCH Verlag. (Sep. 01) (2015), https://doi.org/10.1002/cssc.201500231.

[73] S. Hussain, J.U. Rehman, First-principles calculations to investigate structural, electronics, mechanical, and optical properties of $KGaO_3$ cubic perovskite for photocatalytic water-splitting application, Optik (Stuttg) 291 (2023) 171326, https://doi.org/10.1016/J.IJLEO.2023.171326.

[74] J. Graetz, New approaches to hydrogen storage, Chem. Soc. Rev. 38 (1) (2009) 73–82, https://doi.org/10.1039/b718842k.

[75] M. El Akkel, H. Ez-Zahraouy, Novel double hydride perovskites $Li_2TiF_{6-x}H_x$ as efficient materials for solid-state hydrogen storage: DFT insights, Int. J. Hydrog. Energy 101 (2025) 1406–1420, https://doi.org/10.1016/j.ijhydene.2025.01.023.

[76] V. Kudiiarov, J. Lyu, O. Semenov, A. Lider, S. Chaemchuen, F. Verpoort, Prospects of hybrid materials composed of MOFs and hydride-forming metal nanoparticles for light-duty vehicle hydrogen storage, Appl. Mater. Today 25 (2021) 101208, https://doi.org/10.1016/J.APMT.2021.101208.

[77] W. Khan, M.K. Masood, The investigation of rubidium-based hydrides for hydrogen storage application: density functional theory study, Mater. Sci. Semicond. Process. 173 (2024) 108149, https://doi.org/10.1016/J.MSSP.2024.108149.

[78] D.P. Broom, C.J. Webb, G.S. Fanourgakis, G.E. Froudakis, P.N. Trikalitis, M. Hirscher, Concepts for improving hydrogen storage in nanoporous materials, Int. J. Hydrog. Energy 44 (15) (2019) 7768–7779, https://doi.org/10.1016/j.ijhydene.2019.01.224.